Article:

Kane, IA, Ponten, A, Vangdal, B et al. (3 more authors) (2017) The stratigraphic record and processes of turbidity current transformation across deep-marine lobes. Sedimentology, 64 (5). pp. 1236-1273. ISSN 0037-0746

https://doi.org/10.1111/sed.12346

The stratigraphic record and processes of turbidity current transformation across deep-marine lobes

Ian Kane[1*], Anna Pontén[2], Brita Vangdal[3], Joris Eggenhuisen[4], David M. Hodgson[5], Yvonne T. Spychala[5,4]

[1]*Statoil ASA, Exploration, NO-1364, Oslo, Norway*

[2]*Statoil ASA, Research Centre Rotvoll, NO-7005 Trondheim, Norway*

[3]*Statoil ASA, Research Centre Bergen, NO-5020, Bergen, Norway*

[4]*Faculty of Geosciences, Utrecht University, PO Box 80021, 3508TA Utrecht, The Netherlands*

[5]*School of Earth and Environment, University of Leeds, LS2 9JT, United Kingdom*

**Present address: School of Earth, Atmospheric and Environmental Sciences, University of Manchester, Oxford Road, Manchester M13 9PL, United Kingdom*

Abstract

Sedimentary facies in the distal parts of deep-marine lobes can diverge significantly from those predicted by classical turbidite models, and sedimentological processes in these environments are poorly understood. This gap may be bridged using outcrop studies and theoretical models. In the Skoorsteenberg Fm., a downstream transition from thickly-bedded turbidite sandstones to argillaceous, internally layered hybrid beds is observed. The hybrid beds have a characteristic stratigraphic and spatial distribution, being associated with bed successions which generally coarsen- and thicken-upwards reflecting deposition on the fringes of lobes in a dominantly progradational system. Using a detailed characterisation of bed types, including grain size, grain fabric and mineralogical analyses, a process-model for flow evolution is developed. This is explored using a numerical suspension capacity model for radially spreading and decelerating turbidity currents. The new model shows how decelerating sediment suspensions can reach a critical suspension capacity threshold beyond which grains are not supported by fluid turbulence. Sand and silt particles, settling together with flocculated clay, may form low yield-strength cohesive flows; development of these higher concentration lower boundary layer flows inhibits transfer of turbulent kinetic energy into the upper parts of the flow ultimately resulting in catastrophic loss of turbulence and collapse of the upper part of the flow. Advection distances of the now transitional to laminar flow are relatively long (several km) suggesting relatively slow dewatering (several hours) of the low yield strength

flows. The catastrophic loss of turbulence accounts for the presence of such beds in other fine-grained systems without invoking external controls or large-scale flow partitioning, and also explains the abrupt pinch-out of all divisions of these sandstones. Estimation of the point of flow transformation is a useful tool in the prediction of heterogeneity distribution in subsurface systems.

Keywords: Hybrid beds, transitional flow deposits, flow transformation, deep-marine channels and lobes, reservoir quality, flow capacity, Karoo

Introduction

Observation and interpretation of sedimentary facies from deep-marine lobe deposits has been strongly influenced by models developed from relatively small and coarse-grained basins, for example the Annot sub-basins (Bouma, 1962) and the Californian Borderlands (Lowe, 1982). However, today's ultra-deep-water subsurface exploration targets are typically associated with sedimentary systems that are up to orders of magnitude larger, drained much larger areas, and are significantly finer grained (e.g. the Wilcox Fm. of the Gulf of Mexico, Zarra et al., 2007). The sedimentary environments and facies distributions of these systems are understudied as they commonly develop on passive margins and may overlie transitional or oceanic crust, and as such are prone to subduction. Numerous studies have documented these systems from remote sensing-based observations and slightly more limited core data from the modern and Holocene stratigraphy (an excellent example being the Mississippi Fan, see summary in Twichell et al., 2009). Due to the paucity of outcrops revealing such systems, it may be appropriate to use fine-grained systems in smaller basins as process analogues to larger systems (e.g. Martinsen et al., 2000; Sullivan et al., 2000). In these fine-grained systems, complicated facies and facies distributions, which diverge significantly from classical turbidite models, are reported from medial and distal lobe settings (Haughton et al., 2003, 2009; Sylvester & Lowe, 2004; Talling et al., 2004, 2012; Amy & Talling, 2006; Ito, 2008; Barker et al., 2008; Davies et al., 2009; Hodgson, 2009; Kane & Pontén, 2012; Pyles & Jennette, 2012; Talling, 2013; Grundvåg et al., 2014; Terlaky & Arnott, 2014; Fonnesu et al., 2015; Southern et al., 2015, 2016; Spychala et al., in revision). Such beds have been termed hybrid event beds by Haughton et al. (2009), which emphasises that an individual bed represents the deposits of different types of flow within the same event. Typically, this is a basal turbidite and an upper debrite; the term has, however, been adopted to cover a wide range of deposit and process types which combine to form a single 'hybrid' bed (e.g., Hodgson, 2009; Talling, 2013; Fonnesu et al., 2015). The stratigraphic and spatial complexity of these bed types means that deep-marine fan systems represent significant challenges for reservoir prediction at both exploration and development scales (Porten et al., in press). The Paleogene Wilcox Fm. exemplifies these challenges: it is characterised by extremely large volumes of sandstone, but often occurring as mud-rich sandstones with marginal reservoir quality (i.e., low porosity and permeability values), with stratigraphically and spatially isolated higher-quality reservoir sandstones (Zarra, 2007; Kane and Pontén, 2012).

In this contribution, the spatial and stratigraphic distribution of the various sedimentary facies associated with proximal, medial and distal deep-marine lobe environments of Fan 3, Skoorsteenberg Fm., Tanqua Karoo, are presented and characterised, with particular emphasis on hybrid beds. The paper comprises two interlinked sections, with the main focus being 1) to characterise fine-grained hybrid beds, and 2) to develop a process based numerical model for their observed occurrence. In the first part, we use outcrop and petrological observations to infer sedimentological flow processes. In the second part, a numerical model is introduced to investigate the inferred processes. The model uses a suspension-capacity model (Eggenhuisen et al., 2016), and applies it to radially spreading decelerating flows. Integrating the detailed bed characterisation and the numerical model, we propose that these types of hybrid beds form due to the loss of turbulence due to flow deceleration, the development of internal stratification and eventual catastrophic loss of turbulence in the flow. Understanding of the process sedimentology of these deposits and their stratigraphic and spatial distribution can be applied to systems of similar grain-size range to significantly reduce subsurface uncertainty and to improve prediction.

Data and Methods

The dataset comprises 20 sedimentological logs collected in the field and correlated by walking out individual beds (Fig. 1). These logs were collected at 1:20 scale with more detailed logs of individual beds and packages of beds collected at 1:2 scale (Figs. 2-5). Aerial photographs supported field correlation in areas that were difficult to access or were covered (Fig. 2). Data collected include lithology, bed thickness, and palaeocurrent measurements from ripples, flutes and other sole marks. In addition, the equivalent stratigraphic intervals within cores from 7 research boreholes were logged at 1:20 scale (Fig. 3).

Petrographic analysis was performed from 49 orientated thin sections. Although not strongly cemented, point-counting is challenging due to the high degree of compaction and commonly large proportion of clay. For this reason, further analytical work using the QEMSCAN® (Quantitative Evaluation of Minerals by SCANning electron microscopy) was undertaken on 39 samples to quantitatively analyse the mineralogy and texture of different bed types in order to support qualitative outcrop observations. QEMSCAN® uses an FEI Quanta 650F SEM (Scanning Electron Microscope) with two silicon drift energy-dispersive X-ray spectrometers (Pirrie et al., 2004). X-ray and backscattered electron signals are used to image and create quantified mineralogical maps of thin sections with a resolution of 5 μm). Typically, framework mineral grains are isolated within, or coated by, the clay matrix and they can be imaged separately by the QEMSCAN®. These grains can be measured and grain size distributions made from the resultant large datasets (1×10^5 - 2×10^6 grains per section). Grain size is determined according to the long axis, which is automatically measured in thin section. As with traditional thin-section point-counting, this method underestimates grain-size diameter by 11%, or by 0.2 phi units (Johnson, 1994). The smallest grains measured are 5 μm, which does not significantly truncate the fine tail end of the grain size spectrum.

Geological setting of the Karoo Basin, Tanqua Depocentre and Skoorsteenberg Fm.

During the Permian, the Karoo Basin is interpreted as either a retro-arc foreland basin developed inboard of a fold and thrust belt (De Wit and Ransome, 1992; Veevers et al., 1994; Visser and Prackelt, 1996; Visser, 1997; López-Gamundí and Rossello, 1998), or, to subsidence caused by dynamic topography related to subduction (Pysklywec and Mitrovica, 1999; Tankard et al., 2009). The Tanqua depocentre (Fig. 1A) was a topographic ‘low’ developed within the south-western part of the Karoo Basin, and is bound by an oroclinal bend in the Cape Fold Belt, with the Cederberg branch bounding the western margin and the Swartberg Branch bounding the southern margin. The depocentre is filled by sediments of Westphalian (Carboniferous) to Triassic age, which comprise the Karoo Supergroup. These sediments record the late Palaeozoic deepening and then shallowing of the basin (Hodgson, 2009). The Karoo Supergroup is subdivided into the glaciogenic Dwyka Group (Westphalian to early Permian), the marine Ecca Group (Permian) (Fig. 1C) and the non-marine Beaufort Group (Permo-Triassic) (Smith, 1990).

In the Tanqua depocentre, the Ecca Group comprises an approximately 1400 m thick succession of siliciclastic sediments (Wickens, 1994; King et al., 2009). The lower Ecca Group (the

Prince Albert, Whitehill, and Collingham formations) is overlain by >600 m of mudstone and siltstone (Tierberg Fm.; Hodgson et al., 2006), which in turn is overlain by a c.400 m thick fine-grained interval of sand-rich submarine fans, separated by extensive claystone and siltstone intervals, forming the progradational Skoorsteenberg Fm. (Wickens, 1994; Morris et al., 2000; Johnson et al., 2001; Wild et al., 2005; Hodgson et al., 2006, Hodgson 2009; Prélat et al., 2009; Spychala et al., in revision) (Fig. 1). The Kookfontein Fm. overlies the Skoorsteenberg Fm. and is a c.300 m thick succession representing a submarine slope and shelf-edge delta, shallowing-up to deltaic and shoreface deposits (Wild et al., 2009; Poyatos-More et al., 2016).

Skoorsteenberg Fm.

The c. 400 m thick Skoorsteenberg Fm. consists of five fine-grained sandy intervals, interpreted as four submarine fans (Fans 1-4) and an overlying base-of-slope to lower slope succession termed Unit 5 (Bouma & Wickens, 1991; Wickens, 1994; Morris et al., 2000; Johnson et al., 2001; Wild et al., 2005; Hodgson et al., 2006) (Fig. 1). To retain consistency with previous literature, the 'fan' nomenclature is retained, which has been used as a lithostratigraphic term and encompasses a linked system of sandstone and siltstone channel-fills and lobe bodies. Collectively, the lobes of Fan 3 may be regarded as a lobe-complex set (c.f. Prélat et al., 2009). A robust stratigraphic framework for the formation has been established by several field studies (Wickens and Bouma, 1991; Wickens, 1994; Bouma and Wickens, 2001; Johnson et al., 2001; Hodgson et al., 2006; Hodgson, 2009; Prélat et al., 2009; Hofstra et al., 2015). This has been augmented by seven research boreholes and together this has allowed the development of a detailed evolutionary model for the fan intervals (Hodgson et al., 2006; Luthi et al., 2006). Fan 3 is interpreted to record a pattern of initiation, followed by progradation and aggradation, to retrogradation (Hodgson et al., 2006). Within a sequence stratigraphic framework, each fan has been interpreted to represent a lowstand systems tract and the overlying regional claystone and siltstone as the combined transgressive and highstand systems tract (Goldhammer et al., 2000; Johnson et al., 2001; Hodgson et al., 2006). The chronostratigraphic framework for the fans remains poorly constrained, although recently published U–Pb single-grain zircon ages from volcanic ash layers indicate an overall late Permian age (c.255 Ma, Fildani et al., 2007, 2009; McKay et al., 2015).

Lithofacies of the submarine fans have been described previously (Morris et al., 2000; Sullivan et al., 2000; Johnson et al., 2001; van der Werff and Johnson, 2003a, 2003b; Hodgson et al., 2006; Hodgson, 2009; Prélat et al., 2009; Groenenberg et al., 2010; Jobe et al., 2012; Hofstra et al., 2015). This study focuses on hybrid beds within Fan 3, which have been described previously as biand tri-partite turbidites with slurry or debris flow caps (Morris et al., 2000; Johnson et al., 2001; Hodgson et al., 2006; Luthi et al., 2006). Hodgson (2009) expanded on this work and interpreted these beds as 'hybrid beds' (equivalent to 'hybrid event beds' *sensu* Haughton et al., 2009). Hodgson (2009) interpreted the upper parts of these composite beds as 1) the deposits of debris-flows derived from partial flow transformation after shelf-edge collapse; 2) developed through flow transformation from turbidity currents entraining a muddy substrate; or 3) representing the mudstone clast-rich tails of turbidity currents where the matrix was not argillaceous. Johnson et al. (2001) and Hodgson et al. (2009) noted a preferential geographic distribution of these beds at the fringes of lobe deposits, with Hodgson (2009) attributing a preferential stratigraphic distribution at the base of lobe complexes to slope incision during fan initiation and progradation phases.

Results

Lithofacies

The lithofacies presented here represent 'event beds' and are classified based on outcrop observations (Figs. 2-7) following the approach of Johnson et al. (2001), Hodgson et al. (2006) and Hodgson (2009), utilising the latter's four-fold lithofacies scheme, which is particularly relevant to the fringe facies of lobes. The detailed characterisation of samples from individual beds, presented below is used to support the necessary degree of interpretation of features from outcrop, e.g., mud content (n.b. 'mud' is used here as a general term for mixtures of clay, silt, organic fragments and clay flocs and clasts). Nevertheless, outcrop-based observations/interpretations of relative clay-content closely match quantitative data from analytical techniques, giving confidence in this approach. Therefore, the analysis below is based on outcrop and core observations and provides a framework for the more detailed analyses that follow.

Thick-bedded sandstones (0.6-6 m)

Thick-bedded sandstones are very-fine to fine-grained, generally lacking primary structures but may be marked by dewatering structures, predominantly pillars and lesser dishes; these are subtle features at outcrop and are more clearly visible in core (Fig. 8H). These 'beds' are often amalgams of several beds (e.g., capping Lobe 5, Fig. 2A and C; and Log SK3, Fig. 4). Bed amalgamation can be enigmatic in outcrop, but is more readily observed in core, where typical features comprise mudstone rip-up clasts, subtle grain size changes and truncated dewatering structures. Rarely, bed tops preserve some tractional structures, plane parallel-lamination and ripple cross-lamination, in conjunction with a normal grading profile. Bed bases are sharp, and commonly truncate underlying beds in angular steps (Fig. 6B). Flutes and tool marks are present, but not common. It is less common to see loading at the bases of these thick beds than the thinner-bedded sandstones.

Interpretation: Characteristic features of turbulent flow, such as flutes, tools, normal grading and tractional structures suggest that these beds are turbidites. The general lack of structure throughout most of these beds might in part reflect the often pervasive dewatering, which is apparent in core, but generally not at outcrop. Hodgson (2009) suggests that the overall fine grain size, and its narrow range, preclude the interpretation of flow concentration and sub-division into low-, medium- or high-density turbidites, although tractional structures are generally well developed in many of the thinner turbidites. Based on the observations above and the further discussion of mineralogical and textural data presented below, these deposits are interpreted for the most part as high-density turbidites, *sensu* Lowe (1982).

Thin-to-medium bedded sandstones (0.1-0.6 m)

Very-fine to fine-grained sandstones are generally normally-graded and dominated by tractional structures (ripple- and plane-parallel lamination) (e.g., see Log SK5, interval 7-9 m); in outcrop tractional structures can be very subtle (Fig. 8A). The lower parts of beds may be structureless. Bed bases are sharp, flat lying, and may be marked by flute casts, whilst bed tops may contain abundant organic material and mudstone clasts in a clean sand matrix, and may preserve ripple forms. Banding occurs in some parts of the fan, but can be difficult to discern in the field, being clearer in core (Fig. 8F).

Interpretation: Based on their tractional structuration, normal grading and flute casts, beds of this lithofacies are interpreted as low- to medium-density turbidites deposited by low- to medium-concentration turbidity currents (*sensu* Lowe, 1982). Banding may reflect some periodic suppression of turbulence associated with flow deceleration or increased concentration (Lowe & Guy, 2000; Barker et al., 2008).

Siltstones and thin-bedded sandstones (individual beds <0.1 m)

This lithofacies comprises siltstone to very-fine grained sandstone beds that are commonly interbedded (e.g., interval 1.5-2.5 m, Log Sk20, Fig. 4; Fig. 7). These are typically normally-graded, plane-parallel laminated and/or ripple cross-laminated and sometimes have small flute and tool marks on their bases. In the distal parts of lobes (Prelat et al., 2009) climbing ripple lamination, common in proximal areas, is not observed.

Interpretation: Their tractional structuration and normal grading leads to an interpretation of these beds as turbidites deposited by low-density turbidity currents (*sensu* Lowe, 1982).

Hybrid beds

The focus of this study is the character and prevalence of hybrid beds in frontal lobe fringe deposits (sensu Spychala et al. in revision). Frontal fringe here denotes the distal and frontal part of the lobes, approximately 5 km from their pinch-out, following and consistent with Hodgson (2009) and Prélat and Hodgson (2013), and approximately 25-30 km downdip from the channelized to unconfined areas. In contrast, lateral lobe fringes have rare hybrid beds and are dominated by low-density traction-dominated turbidites (Spychala et al. 2016; in revision).There is a wide range of lithofacies within the hybrid-bed class, and these can be laterally variable within individual beds over the scale of tens of centimetres (Fig. 7). There is a general down-flow progression from deposits that appear more turbiditic to deposits with the character of debrites.

Thick-bedded hybrid beds (0.6-1.2 m)

These occur approximately 5 km from pinch-out. Commonly, thick (up to 1.2 m) beds with stepwise basal erosional cuts (cm-decimetre scale) into the substrate that lack loading and other soft-sediment deformational structures (e.g., bed at 5.4 m SK5, Fig. 4). Beds are generally graded throughout with upper parts that are slightly more clay rich (c. 5-10%, see mineralogy section) and commonly clast rich. These are similar to the thick-bedded turbidites described above but form part of a continuum with the deposits described below, characterised by increasing mud content at bed tops.

Interpretation

In the channel-fills and scour-fills at and beyond the channel-lobe transition (e.g., Hofstra et al., 2015), erosion and entrainment of the weakly consolidated substrate resulted in sharp basal surfaces to turbidites, and the incorporation of intrabasinal clasts. This erosional behaviour seems to have persisted across much of the proximal and medial part of the lobes, at least associated with the larger events, to these relatively distal positions. Entrained substrate was rapidly broken up within the flow often resulting in clast and clay-rich divisions at bed tops. The absence of soft-sediment deformation structures in the underlying substrate is interpreted to be due to excavation of the soft substrate to a firm layer where the substrate shear strength is greater than that of the shear stress exerted by the overriding flow.

Thin- to medium-bedded hybrid beds (0.1-0.6 m)

These occur approximately 3 km from pinch-out. Beds in this 'position' are complicated, with intensely loaded bases and flame structures. Beds are a few to 60 cm thick, but pinch and swell as they load into underlying substrate (e.g., bed at 1-2.5 m Log SK1, Fig. 4; 0-1 m Log SK4, Fig. 5; Figs. 7A, 8). Locally, sections of substrate are fully or partially lifted into the bed. A patchy development of internal layering is observed, with cleaner lower sandstone divisions (c. 10-15% clay, see mineralogy section below), and muddier upper sandstone divisions (c. 30-35% clay) that appear intermittently laterally and extend for 10's to 100's of cm. Rare thin silty caps are observed.

Interpretation

The description demonstrates interaction of an overriding flow with the substrate that, owing to the lower energy of the flows compared to proximal areas, leaves a record of partial or incomplete substrate entrainment. The development of internal layering and the lateral variability suggests that flows increased in concentration but had not developed stable density stratification. The general lack of a silty cap to these beds suggests that the material was mixed within the argillaceous upper parts of these beds and that the flows were undergoing transformation.

Thin-bedded hybrid beds (<0.1 m)

These occur predominantly <1 km from pinch-out. Typically, bi- or tri-partite beds, although some beds have four internal divisions (Figs. 7 & 8). From the base these divisions are: 1) a very-fine-grained sandstone, which is relatively mud-poor with respect to the upper divisions, and always lacking macroscopic tractional structuration. The boundary with the overlying division is typically sharp and may be marked by bed-parallel mudstone clasts; 2) an argillaceous sandstone with a bed-parallel or inclined shear fabric (Fig. 7); 3) a highly argillaceous sandstone with high organic fragment content and a strongly sheared fabric; 4) rare examples have a siltstone cap. Additional internal divisions of variable mud content are common and these typically have the characteristic sheared appearance noted above. In outcrop, mud content is qualitatively determined by colour and weathering style, with muddier beds typically having a more 'bulbous' nature or spherical weathering pattern typical of homogenous rocks. Bed bases are flat to slightly undulose in distal localities, sometimes slightly loaded with rare, small (mm-scale) flame structures.

Interpretation

The high mud content of these deposits suggests deposition from higher concentration flows than their up-dip equivalents, which were depositing en-masse and potentially behaving as transitional to laminar flows. The strong internal layering of these deposits is interpreted to reflect the development of discrete rheological zones within the flow in response to radial spreading of flows, deceleration, and increase in near bed flow concentration. The lowermost sand layer shows no evidence for deposition by turbulent flow, being devoid of erosional or tractional structures with the exception of rare grooves or tool marks, and has a high matrix content (see mineralogy section). Instead, the sandier part of the bed is interpreted to represent the deposit of a high-concentration flow where yield strength was the principal particle support mechanism. The basal layer is typically relatively cleaner than the overlying layer(s) which may reflect the ability of the coarser particles in the flow to settle to its base, suggesting the flow had relatively low strength (e.g., Sumner et al., 2009; Talling, 2013). Clasts along the intra-bed boundaries may represent kinetic sieving, with the larger clasts working their way to the top of the lowermost bed division due to grain collisions in the low strength transitional to laminar flows; alternatively, as grain collisions become less important (i.e., at higher concentrations) buoyancy may have become more important. Upper bed divisions are interpreted to be debris-flow deposits, based on their poor sorting and high matrix content (see *Mineralogy* section below), suggesting a complete flow transformation took place. These divisions are interpreted to reflect, in part, a longitudinal flow structure, rather than representing the one-to-one vertical structure of the flow.

Mineralogy

Results:

Chemical and petrological analysis of thin sections has allowed the mineral composition of the different facies types to be determined (Figs. 9-12). On a quartz-feldspar-lithic ternary diagram the samples plot as lithic arkoses and feldspathic litharenites. An outcrop subdivision of samples into ‘turbidites’ and ‘hybrid beds’ shows that turbidites fall entirely within the lithic arkose class, whilst hybrid beds span the lithic arkose and feldspathic litharenite classes (Fig. 9). The wide range of mineral types identified (Table 1 and Figs. 10 & 11) have been grouped together, for the purpose of examining bed-scale mineralogical variability, into the following three classes, which together form >90% of each sample: 1) quartz, 2) feldspar, and 3) clay. Of the clays, illite is most abundant; from petrological analysis this appears to be primarily detrital in origin, although it could have been altered from another detrital clay form, most-likely smectite or kaolinite; in either case it does not appear to be a diagenetic mineral. In addition to detrital illite (or clay in general), there could be a much smaller contribution from alteration of muscovite or feldspar (Fig. 12). The analysis reveals distinctive mineralogical trends for the hybrid beds and turbidites (Fig. 13). Quartz is the dominant detrital mineral, with slightly lower proportions of feldspar. Muscovite mica represents only 1-2% of the mineral volume with no significant variability between hybrid beds or turbidites (Table 1). Overall quartz is more abundant by proportion in the turbidites than in the hybrid beds, whereas feldspar content remains approximately the same in both bed types (e.g., samples F and G; Fig. 13). Clay content increases from bed bases to bed tops, with values in the lower parts of hybrid beds in the range of 20-25%, compared to around 10% at the base of turbidites; this rises to 25-35% and 20-25% respectively (Fig. 13).

Interpretation:

Compositional differences between hybrid beds and turbidites show a higher lithic content in the former, which partly reflects the higher proportion of mudstone and siltstone clasts incorporated within the hybrid beds. There is no significant difference in the heavy mineral distribution, suggesting that flows across the lobes had a common source. The confirmation of higher mud content in argillaceous divisions of hybrid beds validates the qualitative interpretations of mud content based solely on outcrop observations presented both above and in Hodgson (2009). The apparent strong internal layering of the hybrid beds observed at outcrop is clearly demonstrated to be directly linked to mud content that gives good confidence in the interpretation of graphic logs collected during this study. The relatively low clay content of turbidite sands is expected and has been documented in other studies, e.g., Sylvester & Lowe (2004), and is accounted for by the fine sediment being maintained in suspension as the coarser grains settle out.

Grain size

Results:

Grain size was determined using QEMSCAN®. Individual framework grain outlines (quartz and feldspar) were extracted from the matrix material, to provide an overview of the 5-500 µm grain-size spectrum. Grain size is illustrated as simple plots of trends within individual beds (Fig. 13), and as entire grain-size distributions (Fig. 14). Peaks in the range of 200-500 μm are generally either amorphous clay bodies or claystone clasts, and some minor cemented quartz grains. The grain-size distribution curves illustrate the 'skew' of the grain size population, which can be described as positively skewed when the sample has excess fine grained material (fine skewed), symmetrical, when the distribution is even, or negatively skewed when the sample has an excess of coarse material (e.g., Moiola and Weiser, 1968). In broad terms, turbidites have lower and middle divisions characterised by positively skewed distributions, to symmetrical distributions in their upper divisions, whereas hybrid beds are characterised by negatively skewed lower and middle divisions, shifting to more symmetrical distributions in their upper parts (Fig. 15).

Interpretation:

The mean and maximum grain size of quartz and feldspar in turbidites is generally larger than in the hybrid beds, suggesting that flow transformation took place sometime after the larger grains had settled from suspension in turbulent flows. Typically, en-masse sedimentation would give a broad positively skewed distribution, whilst a winnowed deposit, such as a beach sand, would be coarsely skewed (Moiola and Weiser, 1968). The turbidites show a fine skew, indicating sedimentation of the entire grain-size spectrum with minimal reworking, whereas the hybrid beds are coarsely skewed, indicating that they have an excess of coarse grains in them. An explanation for this is that the coarser grains were able to settle through a low yield strength muddy flow, akin to the late stage settling described experimentally by Sumner et al. (2009). The upper parts of these beds, interpreted as the deposits of higher yield strength flows to fully laminar flows, are characterised by symmetrical distributions reflecting the full grain size distribution available during flow and deposition.

Fabric analysis

Grain orientation is constrained using the least-projection method, which is defined as the direction of the two most-closely spaced parallel lines that can be drawn tangentially to the edges of the longest section of a grain (Dapples and Rominger 1945; Baas et al. 2007). Grain-fabric analysis allows inferences of flow conditions to be made where macroscopic structures are not present. Alignment of long axes occurs in most depositional regimes (although not all, see review by Baas et al. 2007). The samples are devoid of macroscopic tractional structuration meaning that problems regarding the orientation of long-axes with regards to palaeoflow, such as the presence of flow-oblique fabrics or flow-transverse fabrics (typical of ripple cross-lamination), are avoided (see Hiscott & Middleton 1980; Baas et al. 2007, and references therein). The purpose of the analysis is to compare relative grain-fabric differences between bed divisions in individual beds, as this may yield information about the depositional conditions and syn-depositional shearing of the bed. It is stressed that although the sample orientation is consistent for individual beds (parallel to bedding), the orientation with respect to palaeoflow is constrained only by the overall orientation of Fan 3 (e.g. Hodgson et al. 2006; Luthi et al. 2006; Prélat et al. 2009). Grain alignment is influenced by section orientation with respect to palaeoflow, which potentially differed between divisions in individual beds. Nevertheless, the approach gives some support to observations and inferences made in the field, and provides a relative comparison between bed divisions, which is the principal utility here. Long axes were recorded using an automated QEMSCAN® process, meaning that a large number of samples can be analysed quickly (1-2 orders of magnitude more grain measurements than typical manual thin-section fabric studies, e.g., Kane et al., 2010a).

Results:

With one exception, samples from hybrid beds show Von Mises type distributions (normal circular distribution) with vectorial concentrations (K, a measure of mean vector strength) in the range of 0.17-0.75, with a mean value of K = 0.5. In contrast, turbidites are characterised by Von Mises and uniform distributions, distributions with low K values, from 0.04-0.6 with a mean value of K=0.26 (Table 2 and Fig. 13).

Interpretation:

Hybrid beds have a strong grain orientation in comparison to the turbidites (Fig. 13); this fabric is attributed to shearing within the cohesive flow. The low K values for the turbidites support their origin as deposits from high-density turbidity currents where sediment deposition to the bed precluded significant bedload transport or grain organisation. Deposits of low-density turbidity currents, reported in a previous study by Kane et al. (2010a), have better organisation than these deposits with Von Mises and Gaussian (non-circular) distributions, illustrating grain organisation by tractional processes. The strong fabric reported for these hybrid beds suggests that the high-concentration flows, to which they are attributed, were still relatively fluidal with internal shear layers along which elongate grains are aligned.

Stratigraphic and spatial distribution of bed types

Typically, the Fan 3 stratigraphic succession is marked at its base by silty low-density turbidites, which progressively thicken and coarsen upwards from fine siltstones to very-fine sandstones (Figs. 4 & 5). In some places, the first medium to thick beds occur abruptly at the base of the sandy part of Fan 3, and are then overlain by several variably well-developed thickening- and coarsening-upward packages, which are interpreted to represent the individual lobe deposits (Fig. 2). Bed thickness patterns are, however, variable (Prélat and Hodgson, 2013). Fine-scale mapping and correlation by Prélat et al. (2009) led to extensive thin-bedded successions being treated as distinct elements, and were interpreted as the distal fringes of lobes (Prélat and Hodgson, 2013), implying a pronounced compensational stacking pattern. Hybrid beds are found within the lower to middle part of the Fan 3 succession in the distal areas, and are interbedded with turbidites. Within the turbidite succession described above the hybrid beds stack from the distal-, to medial to proximal lobe fringe types described above (Figs. 4 & 5). Interbedded throughout the succession are packages of thin-bedded sandstone and siltstone low-density turbidites. High-density turbidites, and thick-bedded turbidites of uncertain affinity, are well developed in the feeder channel-fills, axial and off-axis areas of the lobes, down-dip of scours and in association with channelised features developed across the lobes; they generally occur at the top of individual lobe stratigraphic units, but can occur at their bases (Morris et al., 2000; Johnson et al., 2001; Hodgson et al., 2006).

Interpretation

The character of flows passing over the Fan 3 lobes can be subdivided into turbidity currents, which deposited a range of low- to high-density turbidites, and the higher concentration transitional or laminar flows inferred above, which deposited hybrid beds. Low-density turbidites are common across all environments and tend to increase in proportion and thin towards the distal pinch-out (e.g., Morris et al., 2000). The low concentration and relatively low degree of density stratification of the flows allowed them to traverse gentle gradient changes associated with depositional relief across the lobes (Groenenberg et al., 2010). High-density turbidites and transitional to laminar facies were deposited by high-concentration flows, and appear to have been strongly controlled by topography related to previous deposits (Groenenberg et al., 2010). High-density turbidites are related to the main feeder channels and low-relief distributary channels developed across the lobe (e.g., Morris et al., 2000; Johnson et al., 2001; Hodgson et al., 2006), and may be the expression of the flows that cut major scours in the channel lobe transition zone (e.g., Hofstra et al., 2015). The flows that deposited these facies are thought to have been strongly density stratified; as such, individual large magnitude flows were able to make their own pathway(s) following depositional topography of precursor lobe deposits and developing ‘finger-like’ bodies across the lobe (Groenenberg et al., 2010). Simple trends of bed thickening associated with lobe progradation, which might be expected in the simplest case (e.g., Mutti and Sonnino, 1981), are obscured by the juxtaposition of thicker beds marking either the onset of a new lobe (but not always), or occurring apparently randomly within an otherwise thickening (or thinning) upwards trend. Nevertheless, the hybrid beds are for the most part associated with medial and distal lobe frontal fringe environments (cf. Spychala et al., in revision), and are developed down-dip of high-density turbidites. Stratigraphically, therefore, the hybrid beds typically occur in the basal parts of lobe successions (Hodgson, 2009). In addition, they can occur in packages representing only the distal fringe of a lobe, i.e., in areas where the sandier parts of the lobe did not reach (e.g., Log Sk4, Fig. 5). The point where transformation occurs is the subject of the following section.

Discussion

Fan 3 turbidity currents and flow transformation

Whilst much of the Fan 3 stratigraphy is dominated by turbidites, sedimentary facies tracts and stratigraphic stacking suggest that some turbidity currents transformed to transitional or laminar flows (e.g. McCave & Jones, 1988; see review by Talling, 2013). This interpretation is based on the downstream facies transitions described above, whereby turbidites pass downstream into hybrid beds. The ability of a turbidity current to maintain sediment in suspension is affected by lateral spreading and associated deceleration; we postulate that this alone can force local flow transformation, resulting in deposition of a hybrid bed in the distal parts of a lobe.

The analysis utilises the suspension capacity parameter Γ (Eggenhuisen et al., 2016), a measure of a flow’s ability to maintain sediment in suspension, in conjunction with a geometrical model of flow expansion. A simple numerical model is developed to show how Γ evolves as a turbidity current spreads laterally and decelerates across a lobe. In this discussion, a ‘lobe’ scale is used rather than a ‘lobe element’ as the latter are less well-constrained. The suspension capacity parameter Γ represents a force balance between the downward gravity force, F_g, and upward directed turbulent forces(F_{turb}) that can be used to compare dynamic turbulence scales to gravitational scales acting near the base of turbidity currents. F_g is the net force resulting from buoyancy and gravity acting on sediment grains in suspension. The turbulent force scale F_{turb} is derived from universal scaling of turbulent Reynolds-stress gradients in the region just above the bed where turbulent structures are generated that export excess turbulent kinetic energy that cannot be dissipated in the boundary layer upward into the flow (Pope, 2000). This region will be a few millimetres to centimetres thick in a typical turbidity current. The suspension capacity parameter Γ is given by (see Eggenhuisen et al. [2016] for a full derivation):

$$\Gamma = \frac{F_{turb}}{F_g} = \frac{u_*^3}{140 v g R C_b} \qquad (Equation\ 1)$$

Where u_* is the shear velocity, v is the kinematic viscosity of water (1.002 10^{-6} m^2/s), g is the constant of acceleration by gravity, C_b is volumetric sediment concentration near the bed, and $R = (\rho_s - \rho_f)/\rho_f$ is the relative density of sediment where ρ_s and ρ_f are the particle and fluid density respectively (2650 kg m^{-3} for quartz and 1020 kg m^{-3} for seawater) giving R = 1.6. The numerical constant 140 derives from universal scales of vertical turbulence in boundary layer flow (Eggenhuisen et al., 2016).

Near-bed turbulence dominates suspension when $\Gamma > 1$, and the turbulent conditions could maintain more sediment in suspension, such that, additional sediment can be entrained into the passing flow if it is readily available at the bed. This condition is therefore termed under-saturated with respect to the turbulent suspension capacity of the flow. At $\Gamma = 1$, turbulent forces near the bed are equal to the gravitational pull on the suspended particle load. This force balance prevents average net vertical acceleration of the sediment particles and the fluid between them, and the flow is in saturation equilibrium with suspended sediment near the boundary; in this condition C_b can be seen as a saturation concentration.

Gravity dominates suspension when $\Gamma < 1$ and the upward turbulent forces are smaller than downward gravitational forces applied to the fluid by the particles, this prevents turbulent accelerations and results in turbulence extinction. This condition is termed over-saturated with suspended sediment because the flow does not have sufficient turbulent capacity to suspend all the particles present near the bed. A recent breakthrough in DNS simulations of turbidity currents (Cantero et al., 2009, 2011, 2012) demonstrates how turbulence production at the base of turbidity currents is shut-down rapidly in over-saturated suspensions, leading to rapid laminarization extending upwards in the flow. The result will be increasing sediment stratification towards the base of flow as there is no mechanism to counter the gravitational settling of sediment. A key outcome of the work by Cantero et al. (2009, 2011, 2012) and Eggenhuisen et al. (2016) is that extinction of turbulence can occur at very low absolute concentrations of suspended sediment. The conventional perception that turbulence suppression occurs at high sediment concentrations is only true in very high energy flows. Low concentrations suffice to fully suppress turbulence generation in moderate or gentle flow conditions. Occurrence of hindered settling at sufficiently high sediment concentrations can slow down and delay sediment accumulation rates to the base of the flow, but cannot stop sediment in a laminarized flow from settling completely.

Equation 1 is coupled to a model describing the structure of an oversaturated turbidity current spreading over a lobe, after exiting a channel mouth to investigate the evolution of Γ in the spreading flow. Estimation of the suspension capacity parameter depends on an estimation of the shear velocity from the flow scales:

$$u^* = \sqrt{gH\bar{C}RS} \qquad \textit{(Equation 2)}$$

Where $\overline{C}$ is the depth averaged concentration, H is the flow thickness [m] (see discussion below), and S is the tangent of the slope [-]. in the model output, the turbidity current exiting the channel is followed while it spreads out over the lobe. The flow is considered uniform, and its bulk discharge is conserved, such that the product of depth averaged flow velocity, flow thickness, and flow width W is constant as the current travels in direction x along the lobe:

$$Q_b = H(x)\overline{U(x)}W(x) = constant \qquad \textit{(Equation 3)}$$

A drag coefficient C^d is used to set a fixed ratio between the average velocity and shear velocity:

$$C^d = U/u^* \qquad \textit{(Equation4)}$$

The value of the drag coefficient C^d is set to 0.005 (following Parker et al., 1987). Essentially, this model describes a depth averaged flow structure at different positions during passage over a lobe assuming that friction always balances gravitational driving force. The different positions are linked by the volumetric requirement that all discharge debauched from the input condition of the channel mouth is spread equally over the lobe surface by lateral spreading, not by consideration of energy in the form of momentum changes, potential energy losses, or variations in the budget of turbulent kinematic energy. This analysis is thus cruder than depth averaged simulations that solve such energy equations. The purposeful simplicity of this model makes the system easy to investigate and robust to the interrogation of first order controls on the flow structure with distance.

The main simplifying assumptions on the behaviour of the turbidity current are: there is no erosion or deposition as source or sink terms in Eq. 3 (constant discharge). Slope gradient is constant, not some decreasing function S(x) of along-lobe distance x. The drag coefficient is constant in Eq. 4, and does not change with changing friction against the ambient water. The flow spreads out equally over the lobe surface, and does not focus in preferential flow pathways. The effect of these simplifying assumptions will be discussed following the main result.

The discharge can be expressed purely as a function of the flow geometry by substituting Eq.4 and Eq.2 into Eq.3:

$$Q_b = \frac{\sqrt{g\bar{C}RS}}{\sqrt{C_d}} H(x)^{1.5} W(x) \qquad \textit{(Equation 5)}$$

The geometries of the channel deposits in the proximal areas of Fan 3 are used to constrain the flow dimensions that fed from channels onto the lobe surfaces. Channel depth (h) is used as a proxy for flow thickness (H); in Fan 3, channel depths (in the proximal parts of the stratigraphy) are in the range of 5-13 m (e.g. Sullivan et al. 2000, from the Ongeluks River outcrops). This approach provides a minimum value for flow thickness (e.g., El-Gawad et al., 2012) as flows may be significantly super-elevated above the channel depth (e.g., Piper & Normark, 1983, Mohrig & Buttles, 2007, Kane et al., 2010b), however, it is assumed that the channel depth values are within the same order of magnitude as the original flow thickness. In a series of physical experiments, Mohrig & Buttles (2007) demonstrated that over-spilling (super-elevated) channelized turbidity current thicknesses were typically in the range of $h/H \leq 1.3$. The relationship of channel fill thickness to instantaneous channel depth is also not straightforward, but if we assume a minimum depth of 13 m (maximum channel fill thickness) then, if $h/H \leq 1.3$, we have a minimum estimate of H=17 m at the lobe apex (i.e., channel to lobe transition area), negating burial compaction effects. Groenenberg et al. (2010) estimated a thickness of 4 m based on the height of depositional relief in the medial to distal parts of the lobe. Lobe width (W=15 km) is used as a proxy for the maximum flow width and lobe length is taken as 25 km (Prélat et al., 2009). The flow is assumed to spread evenly over the full width of the surface of the lobe, and the width is set to increase linearly from the width of the channel at the lobe apex (250 m) to the full lobe width at a distance similar to the lobe length. The evolution of flow thickness, flow velocity, and shear velocity with distance along the lobe can now be resolved using these assumptions (Fig.16). Flow thickness is equal to the estimate from channel depth at the lobe apex (17 m) and decreases rapidly proximally from 0-5 km to about 4 m thick (corresponding approximately to the values estimated by Groenenberg et al. 2010 for the medial–distal lobe), and more slowly to the lobe termination at 25 km. Flow velocity and shear velocity show similar patterns (Fig. 16B). The evolution of the suspension capacity parameter, Γ, goes through the threshold value of 1, at which point turbulence is supressed at 21km from the lobe apex and 4 km from lobe pinch-out (Fig. 16C).

Discussion of the numerical model

The model demonstrates that a laterally spreading turbidity current, without entrainment of eroded substrate material (or water), will decelerate, thin and lose its suspension capacity as the bed shear velocity decreases. The model is necessarily simple as there are many poorly constrained parameters and spatially variable feedbacks that may obscure the analysis of the first order parameters governing suspension capacity. However, whilst inclusion of such second order effects in the equations presented would modify the predicted flow conditions for the estimated values of slope and channel mouth concentration, and thereby the loci of the flow transformation, the first order result that flow spreading can result in flow transformation in the distal sections of lobes remains. Previous models have suggested flow collapse in a similar manner, but are reliant on the poorly constrained gradient Richardson number (e.g. McCave and Jones, 1988) or the shear Richardson and shear Reynolds numbers (e.g., Cantero et al., 2012). These approaches necessitate the incorporation of grain-size and settling velocity to establish vertical gradients of velocity and concentration, and are dependent on bulk-flow Reynolds numbers. The present model avoids these ambiguities.

The model presented above infers a homogenous and steady longitudinal flow structure, but it can be envisaged that Γ varies spatially within the flow, as well as temporally as demonstrated. This is a necessary simplification for the purposes of this discussion. The overall lobe body is by definition a depositional unit; if the suspension capacity parameter sets deposition this would imply that $\Gamma = 1$ is at the lobe apex/channel mouth. This may be explained by the longitudinal structure of the flows, and the general trend of progradation through time, such that successive flows tend to step farther basin-ward during the growth phase; this may include the precise position of the channel-lobe transition and lobe apex (e.g., Hodgson et al., 2016; de Leeuw et al., 2016).

The longitudinal structure of the flows in terms of Γ may be expressed by the vertical facies stacks in individual lobes. In proximal areas erosion surfaces overlain by relatively clean basal sandstones may indicate that $\Gamma > 1$ during the passage of the head and body, switching to $\Gamma \leq 1$ during deposition of the tail-end of the flow. Distally, muddy sandstones overly conformable bed bases, have a high matrix content and display sheared fabrics, suggesting that basal flow was laminar from the onset at its arrival at distal locations, i.e., $\Gamma < 1$.

The implication of the observed erosion in the proximal lobes suggests that flows exiting the channel mouth were under-saturated ($\Gamma > 1$) but may also be diagnostic of bathymetric control on flow behaviour at the confined-to- unconfined transition, e.g., a hydraulic jump. The purposeful simplicity of the model has the benefit that the effects of the main simplifications can be isolated and analysed.

Erosion and deposition.

The outcrops show evidence for erosion in proximal lobe locations, indicating that material was entrained in the first few to 10 km after a flow exited the channel. Erosion would increase flow volume, concentration and/or thickness, flow velocity, and bed-shear velocity in the proximal section of the lobe to values exceeding those of the scenarios presented in Figures 17 and 18, and thereby delay flow transformation. Deposition of sediment from the laminarised base of the flow down-dip of flow transformation will decrease the amount of sediment in suspension, and thereby bed shear stress, leading to inevitable collapse of the flow. Thus, erosion then deposition can cause the flow transformation point to be located in more distal positions than those indicated by Figures 17 and 18, but would not alter the result that flow spreading is sufficient to force transition to deposition from laminarised flow.

Constant slope.

Slope gradient is a main control on sediment bypass (Stevenson et al., 2015), and bypass-dominated channels tend to form on gradients that are relatively steeper, whilst deposition-dominated lobes tend to form on slopes that are relatively more gentle (e.g., Kneller, 2003). This decrease in slope is not incorporated into the analysis presented above. In addition, the surface is assumed to be smooth whilst in reality a complex topography of older lobe deposits and basin relief will affect the flows (Prélat et al., 2009; Groenenberg et al., 2010; Spychala et al., 2016). Down-dip decrease in slope is expected to decrease the flow capacity over the proximal lobe more rapidly than illustrated in the scenarios of Figures 16 and 17. In addition, aggradational and erosional relief will introduce lateral flow variability and lateral stacking variability (Prélat et al., 2009; Groenenberg et al., 2010).

Constant drag coefficient.

The ratio between drag at the upper surface and the bed on turbidity currents is recognised to vary based on flow conditions (e.g., Parker et al., 1987; Sequeiros, 2012). However, the shift in relative drag is commonly ignored in analyses, as it has been here. At low Richardson scales, mixing at the top of the turbidity current is reduced, which reduces friction at the top when compared to friction at the base of the flow (Kneller et al., in review). This balance is assumed to be constant in the usage of Eq. 4. The bed shear stress is still decreasing monotonically with distance along the lobe, but at a lower rate than the scenarios presented in Figures 16 and 17 when the balance of friction is allowed to shift towards the bed with lower Richardson scales. The effect of this phenomenon is the delay of flow transformation to a more distal location.

Equal spreading over the lobe.

The observed finger-like geometry of Fan 3 and the associated facies distribution is evidence for focussed flow pathways (Rozman 2000; Rozman and Bouma 2000; Johnson et al., 2001; Hodgson et al., 2006; Groenenberg et al., 2010). Consequently, the flow does not cover the lobe equally and flow capacity will be higher along the pathways due to the higher amounts of sediment in suspension, and increased flow velocity increasing the basal shear velocity. On the fringes of these pathways it may be possible that lateral flow may undergo transformations (Spychala et al., in revision).

Flow transformation

Reduction in the flow suspension capacity as described above may lead to the development of a dense, cohesive lower boundary layer flow, where flows are primed to do so (abundance of clay minerals and fine grained sediment). A steady, non-cohesive, low concentration turbidity current has a given capacity, which drops as the flow decelerates (Hiscott, 1994). Accordingly, sediment falls from suspension to the bed to form a grain framework, or 'rigid' bed which may or may not be reworked depending upon the shear stress exerted by the flow on the bed. Sediment suspensions with a significant cohesive and very fine-grained fraction behave differently and have the potential to form fluid beds due to the high water content of clay flocs and fluid trapping by very fine-grained non-cohesive sediment, which may allow the 'bed' to continue to flow (e.g., Winterwerp & Van Kesteren, 2004). Silt and very fine sand may settle into the dense basal layer together with larger clay flocs and other relatively large clasts and grains (mud clasts, micas, organic material). The aggrading dense boundary layer flow, developed in the decelerating and progressively more stratified flow, would therefore be saturated and cohesive, and given the appropriate conditions, would be able to continue flowing downstream as a cohesive flow (rather than settling to form a rigid bed). In such a flow, yield strength and buoyancy may become the primary particle support mechanisms (e.g., Talling, 2013). McCave and Jones (1988) suggest that under these conditions shearing at the lower boundary layer and continuous flux of the ambient fluid may flush the dense lower layer breaking up clay flocs and pushing clay upwards in the flow or mobile deposit. This may give rise to the development of a slightly better sorted thin lower layer, upon which the clay rich suspension rides; and may explain the thin slightly better sorted layer present at the base of most of the hybrid beds deposits documented here. Support for this comes from the presence of mud clasts along intra-bed boundaries between basal relatively clean sandstone and overlying muddier sandstones (e.g. Fig. 7E), suggesting that relative particle buoyancy may have played a role in the lowermost part of the flow.

The minimum yield strength (τ_y) required to support a given grain size (d_{max}) within the inferred transitional to laminar flows can be calculated, following Johnson (1970) and Hampton (1972, 1975):

$$d_{max} = \frac{8.4\tau_y}{(\rho_p - \rho_f)g}$$

(8)

Hampton (1972) demonstrated that this was a reliable approximation for sand particles submerged in a clay-water matrix. To maintain laminar support of 125 μm quartz grains, that equates to a low yield strength, 0.2 Pa. Flow concentrations in the range of 6% kaolin clay would be required to generate the necessary yield strength to support 125 μm quartz grains; concentration is calculated by rearranging Wan's (1982) formula:

$$\tau_y = 1280\left(\frac{C}{100}\right)^3$$

(9)

The empirical formulation of Wan (1982) is only valid for kaolin flows, however, the petrological analysis suggests that the primary clay was most-likely illite, which tends to form stronger bonds than kaolin (see mineralogy section above). Shearing intensity decreases yield strength considerably (Hampton, 1975), therefore the effect of shear stress on these flows also needs to be considered. For example, Sumner et al. (2009) found that concentrations of approximately 14% kaolin were needed to support very fine- to medium-grained sand (63-250 µm) in shearing clay-rich flows; similar figures were suggested from the settling tube experiments of Amy et al. (2006). Additionally, Major and Pierson (1992), in a series of experiments on sand-silt-clay slurries, noted that small changes in sediment concentration, in the order of 2-4%, produced yield strength changes of up to an order of magnitude. The minimum concentration estimate above (6% clay) is within the range of flow concentrations considered by McCave & Jones (1988) (5-10%) for the generation of clay-silt yield strength dominated flows; however the values of Sumner et al. (2009) (~14% clay; albiet kaolin) for shearing fine-sand bearing flows are probably more appropriate.

The advection distance of these flows appears to be in the order of several kilometers, based on bed length, suggesting that dewatering was a relatively slow process. Assuming that the laminar flows intially have the flow velocity of their parent turbidity currents, e.g., for a 5% concentration flow this might be in the region of 0.4 m/s (Figure. 16B), an advection distance of 4 km (from the 21 km 'transformtion point' to the lobe pinch-out) would suggest a dewatering time of c. 2.5 hours. In all likelihood, the average flow velocity is significantly lower. A 0.2 m/s flow would suggest a dewatering time of 5 hours. There is much local varibaility, which likely reflects subtle changes in gradient and orientation with respect to palaeoflow.

Summary and comparison to 'long-distance transformation model'

The Fan 3 hybrid beds are related to events that entrained the substrate. Radial spreading of individual flows and consequent deceleration caused the flow suspension capacity to be overcome, and flows became transitional to laminar. Due to the high proportion of cohesive and fine material, a dense low yield strength flowing layer formed, which progressively shut off the transfer of turbulent kinetic energy from the base of the flow into the upper layers. Following this, the flows rapidly lost energy and consequently come to a rest relatively abruptly, with the cleaner-lower and muddier-upper deposits pinching out approximately contemporaneously. The transformation model is broadly similar to that postulated by McCave and Jones (1988), and Talling's (2013) model 3. The principal difference to Hodgson's (2009) 'D2' model is that the basal sandstones are here not considered to be the product of forerunning turbidity currents, rather they are considered to be the product of distal flow collapse and transformation, although both models rely on incorporation of substrate material updip. As demonstrated by the numerical model, deceleration alone may result in flow transformation (Model 3 of Talling, 2013), but in this case the evidence shows that many of the flows depositing hybrid beds behaved erosively updip when they were undersaturated ($\Gamma>1$), and through deceleration became saturated ($\Gamma<1$) and transformed to transitional-laminar flows.

Transformation appears to be a general characterisitc of decelerating clay-rich flows (Talling, 2013). If the coarser fraction of the flow has not completely settled at the point where viscous forces begin to dominate, these grains will be incorporated into the higher strength flow (Talling, 2013). In the case of the style of distal beds outlined here, and seen elsewhere in systems of a similar grain size, (e.g, the Wilcox Fm. Zarra et al., 2007; Kane & Pontén, 2012), the low settling velocity of the very fine-grained sand and coarse silt, may make these type of deposits common. This is for two reasons: 1) coarser grained flows may undergo sedimentation earlier, without time for the transformation to occur; 2) coarser or denser grains require greater tubulent energy to be supported, and this may inhibit the formation of clay bonds. Consequently, in coarser-grained systems lacking the fine tail, these types of hybrid beds may not develop.

Conclusions

A downstream transition from turbidite-dominated stratigraphy to mixed turbidites and hybrid beds is documented. Hybrid beds from the distal parts of Fan 3 stratigraphy are characterised and placed within a physical model based on application of the suspension capacity parameter, Γ. Flow transformation is inferred to take place through:

1. Erosion and entrainment by turbidity currents of clay, silt and very fine sand in the channel to channel-lobe transition zone areas when flows are undersaturated ($\Gamma >1$)

2. Deceleration of flows is associated with radial spreading from the lobe apex, reduction in bed shear stress and accordingly a reduction in suspension capacity; we present a simple model for estimation of this.

3. Formation of a low yield-strength cohesive basal layer, which flows in a transitional to increasingly laminar manner that allows settling of the denser/coarser grained fraction.

4. The rising yield strength of the lower layer inhibits the efficiency of vertical mixing, leading to a collapse of the turbulent energy field and en-masse transformation of the upper part of the flow. This results in a thick argillaceous sandstone division containing the residual material within the flow (sand, silt, clay, organics, mica grains).

The fine-grained nature of the Fan 3 gravity flow system may have promoted the development of these types of flows, with the fine suspended load transforming to low yield-strength driven flows following loss of suspension capacity; this is potentially the reason that very similar facies are found in other systems of similar grain size range (e.g., Ross Fm., e.g., Pyles & Jennette. (2009), Wilcox Fm., e.g., Zarra (2007)).

Flow transformation is here considered to be localised, occurring due to autocyclic evolution of radially decelerating flows, rather than a long runout process with the constituent parts dividing into a forerunning turbidity current and trailing debris flow (Haughton et al., 2003; 2009; Hodgson, 2009); whilst those models are valid, the model presented herein provides a mechanism for the development of transitional to laminar flows from an initial turbulent flow, and a particular class of layered hybrid bed which seem to dominate fan fringes in fine-grained systems.

Acknowledgements

This research was made possible with the logistical assistance of Steve Flint, Deville Wickens and the staff of Inverdoorn Game Reserve, for which we are grateful. Numerous colleagues at Statoil have given assistance, support and advice in the field and planning stages: Lars-Magnus Fält, Frode Hadler-Jacobsen, Nils Erik Janbu, Stephen Johnson and Carlo Messina are all thanked. Ruth Elin Midtbø is thanked for the thin-section photographs. Zoltan Sylvester is thanked for comments on an earlier version of this manuscript; Peter Haughton and Mauricio Perillo and Associate Editor Peter Talling are thanked for their thoughtful reviews and for guidance which greatly improved the manuscript.

References

Amy, L.A. and Talling, P.J. (2006) Anatomy of turbidites and linked debrites based on long distance (120 × 30 km) bed correlation, Marnoso Arenacea Formation, Northern Apennines, Italy. Sedimentology, **53**, 161-213.

Amy, L.A., Talling, P.J., Edmonds, V.O., Sumner, E.J. and Lesueur, A. (2006) An experimental investigation of sand–mud suspension settling behaviour: implications for bimodal mud contents of submarine flow deposits. Sedimentology, **53**, 1411–1434.

Baas, J.H., Hailwood, E.A., McCaffrey, W.D., Kay, M., and Jones, R. (2007) Directional petrological characterisation of deep-marine sandstones using grain fabric and permeability anisotropy: methodologies, theory, application and suggestions for integration. *Earth-Science Reviews*, **82**, 101–142.

Baas, J.H., Best, J.L., Peakall, J., and Wang, M. (2009) A phase diagram for turbulent, transitional and laminar clay suspension flows. *Journal of Sedimentary Research*, **79**, 162–183, doi:10.2110/jsr.2009.025.

Baas, J.H., Best, J.L., and Peakall, J. (2011) Depositional processes, bedform development and hybrid bed formation in rapidly decelerated cohesive (mud–sand) sediment flows. *Sedimentology*, 58, 1953–1987. doi:10.1111/j.1365-3091.2011.01247.x.

Barker, S.P., Haughton, P.D.W., McCaffrey, W.D., Archer, S.G., and Hakes, B. (2008) Development of rheological heterogeneity in clay-rich high-density turbidity currents: Aptian

Britannia Sandstone Member, U.K. Continental shelf. *Journal of Sedimentary Research*, 78, 45–68, doi:10.2110/jsr.2008.014.

Bouma, A.H. (1962) *Sedimentology of some flysch deposits: A graphic approach to facies interpretation*. Elsevier, Amsterdam, 168 pp.

Bouma, A.H. and Wickens, H.D. (1991) Permian passive margin submarine fan complex, Karoo Basin, South-Africa: possible model to Gulf of Mexico. *Transacations-Gulf Coast Association of Geological Societies*, **41,** 30-42.

Cantero, M. I., Balachandar, S. and Parker, G. (2009), Direct numerical simulation of stratification effects in a sediment- laden turbulent channel flow, *Journal of Turbulence*, 10, 37–41.

Cantero, M.I., Cantelli, A., Pirmez, C., Balachandar, S., Mohrig, D., Hickson, T.A., Yeh, T-H., Naruse, H. and Parker, G. (2012) Emplacement of massive turbidites linked to extinction of turbulence in turbidity currents. *Nature Geoscience*, **5**, 42-45.

Cantero, M. I., Shringarpure, M. and Balachandar, S. (2012), Towards a universal criteria for turbulence suppression in dilute turbidity currents with non-cohesive sediments. *Geophysical Research Letters*, **39**, L14603.

Cole, D.I. (1992) Evolution and Development of the Karoo Basin. *Inversion Tectonics of the Cape Fold Belt, Karoo and Cretaceous Basins of Southern Africa***,** 87-99.

Coulson, J.M. and Richardson, J.F. (1991) Chemical Engineering Vol. 2. Butterworth Heinemann, Oxford. 1183p.

Dapples, E.C., and Rominger, J.F. (1945) Orientation analysis of fine-grained clastic sediments: a report of progress. *Journal of Geology*, **53**, 246–261.

DeCelles, P.G. and Giles, K.A. (1996) Foreland basin systems. *Basin Research*, **8,** 105-123.

De Leeuw, J., Eggenhuisen J.T. and Cartigny, M.J.B. (2016) Morphodynamics of submarine channel inception revealed by new experimental approach. Nature Communication, **7**:10886 doi: 10.1038/ncomms10886

De Wit, M.J., and Ransome, I.G.D. (1992) Regional inversion tectonics along the southern margin of Gondwana. In: Inversion Tectonics of the Cape Fold Belt, Karoo and Cretaceous Basins of Southern Africa. In De Wit, M.J., and Ransome, I.G.D. Rotterdam, Balkema, p. 15–21.

El-Gawad, S. Abd., Cantelli, A., Pirmez, C., Minisini, D., Sylvester, Z. and Imran, J. (2012) Three-dimensional numerical simulation of turbidity currents in a submarine channel on the seafloor of the Niger Delta slope. Journal of Geophysical Research, 117, C05026.

Eggenhuisen, J.T., Cartigny, M.J.B. and de Leeuw, J. (2016). Physical theory for near-bed turbulent particle-suspension capacity. Earth Surface Dynamics Discussion, doi:10.5194/esurf-2016-33.

Fildani A., Weislogel A.,Drinkwater N.J., McHargue T., Tankard A., Wooden J., Hodgson D., Flint S. (2009) U-Pb zircon ages from the southwestern Karoo Basin, South Africa—Implications for the Permian-Triassic boundary. *Geology*, **37**, 719–722. doi: 10.1130/G25685A.1.

Fildani, A., Weislogel, A., Drinkwater, N.J., McHargue, T., Tankard, A., Wooden, J., Hodgson, D. and Flint, S. (2009) U-Pb zircon ages from the southwestern Karoo Basin, South Africa-Implications for the Permian-Triassic boundary. *Geology*, **37,** 719-722.

Folk, R.L., Andrews, P.B. and Lewis, D.W. (1974) Detrital sedimentary rock classification and nomenclature for use in New Zealand. *New Zealand Journal of Geology and Geophysics*, **13**, 937-968.

Fonnesu, M., Haughton, P., Felletti, F., and McCaffrey, W. (2015) Short length-scale variability of hybrid event beds and its applied significance. *Marine and Petroleum Geology, 67, 583-603.*

Goldhammer, R.K., Wickens, H.DeV., Bouma, A.H., and Wach, G. (2000) Sequence stratigraphic architecture of the Late Permian Tanqua submarine fan complex, Karoo Basin, South

Africa, in Bouma, A.H., and Stone, C.G., eds., Fine-Grained Turbidite Systems: American Association of Petroleum Geologists, Memoir 72, and SEPM, Special Publication 68, p. 165–172.

Groenenberg, R.M., Hodgson, D.M., Prelat, A., Luthi, S.M. and Flint, S.S. (2010) Flow-Deposit Interaction in Submarine Lobes: Insights from Outcrop Observations and Realizations of a Process-Based Numerical Model. *Journal of Sedimentary Research*, **80,** 252-267.

Grundvåg, S.A., Johannessen, E.P., Helland-Hansen, W. and Plink-Björklund, P. (2014) Depositional architecture and evolution of progradationally stacked lobe complexes in the Eocene Central Basin of Spitsbergen. *Sedimentology*, **61**, 535-569.

Hampton, M.A. (1972) The role of subaqueous debris flow in generating turbidity currents. Journal of Sedimentary Petrology, **42**, 775–793.

Hampton, M.A. (1975) Competence of fine grained debris flows. Journal of Sedimentary Petrology, **45**, 833–844.

Haughton, P.D.W., Barker, S.P. and McCaffrey, W.D. (2003) 'Linked' debrites in sand-rich turbidite systems - origin and significance. *Sedimentology*, **50,** 459-482.

Haughton, P., Davis, C., McCaffrey, W. and Barker, S. (2009) Hybrid sediment gravity flow deposits - Classification, origin and significance. *Marine and Petroleum Geology*, **26,** 1900-1918.

Hiscott, R.N., and Middleton, G.V. (1980) Fabric of coarse deep-water sandstones, Tourelle Formation, Quebec, Canada: Journal of Sedimentary Petrology, 50, 703–722.

Hiscott, R.N. (1994) Loss of capacity, not competence, as the fundamental process governing deposition from turbidity currents. *Journal of Sedimentary Research*, A64, 209–214.

Hodgson, D., Flint, S.S., Hodgetts, D., Drinkwater, N.J., Johannessen, E.P. and Luthi, S.M. (2006) Stratigraphic evolution of fine-grained submarine fan systems, Tanqua depocenter, Karoo Basin, South Africa. *Journal of Sedimentary Research*, **76,** 20-40.

Hodgson, D. (2009**)** Distribution and origin of hybrid beds in sand-rich submarine fans of the Tanqua depocentre, Karoo Basin, South Africa. *Marine and Petroleum Geology*, **26**, 1940–1956, doi:10.1016/j.marpetgeo.2009.02.011.

Hodgson, D., Kane, I., Flint, S., Brunt, R., Ortiz-Karpf, A. (2016). Time transgressive confinement on the slope and the progradation of basin-floor fans: Implications for the sequence stratigraphy of deep-water deposits. *Journal of Sedimentary Research*, 86, 73-86.

Hofstra, M. Hodgson, D.M. Peakall, J.; Flint, S.S. (2015) Giant scour-fills in ancient channel-lobe transition zones: Formative processes and depositional architecture. *Sedimentary Geology*, Volume 329, 98-114.

Ito, M. (2008) Downfan transformation from turbidity currents to debris flows at a channel-to-lobe transitional zone: the lower Pleistocene Otadai Formation, Boso Peninsula, Japan. *Journal of Sedimentary Research*, **78**, 668–682.

Johnson, A. (1970) Physical Processes in Geology, W. H. Freeman, New York. 577 p.

Johnson, M.R. (1994) Thin section grain size analysis revisited. *Sedimentology*, **41**, 985–999.

Johnson, S.D., Flint, S., Hinds, D. and Wickens, H.D. (2001) Anatomy, geometry and sequence stratigraphy of basin floor to slope turbidite systems, Tanqua Karoo, South Africa. *Sedimentology*, **48,** 987-1024.

Kane, I.A., McCaffrey, W.D., and Peakall, J. (2010a) On the origin of palaeocurrent complexity within deep marine channel levees. Journal of sedimentary Research, **80**, 54-66.

Kane, I.A., McCaffrey, W.D., Peakall, J. and Kneller, B.C. (2010b). Submarine channel levee shape and sediment waves from physical experiments. *Sedimentary Geology*, 223, 75-85.

Kane, I.A. and Pontén, A.S.M. (2012) Submarine transitional flow deposits in the Paleogene Gulf of Mexico. *Geology*, **40,** 1119-1122.

Khelifa, A. and Hill, P.S. (2006) Models for effective density and settling velocity of clay flocs. *Journal of Hydraulic Research*, **44**, 390-401.

King, R.C. (2005) *Structural evolution of the Cape Fold Belt; implications for sediment routing to the SW Karoo Basin*, University of Liverpool, Unpublished, 327 pp.

King, R.C., Hodgson, D.M., Flint, S.S., Potts, G.J. and Van Lente, B. (2009) Development of subaqueous fold belt as a control on the timing and distribution of deepwater sedimentation: An example from the Southwest Karoo Basin, South Africa. In: Kneller, B., Martinsen, O.J., McCaffrey, B. (Eds.), External Controls on Deep-Water Depositional Systems. *SEPM Special Publication,* **92**, 261-278.

Kneller, B. C. (1995) Beyond the turbidite paradigm: physical models for deposition of turbidites and their implications for reservoir potential. In: Characterization of Deep Marine Systems (Eds A.J. Hartley and D.J. Prosser), Geol. Soc. Spec. Publ., **94**, 31–49.

Kneller, B.C. 2003. The influence of flow parameters on turbidite slope channel architecture. *Marine and Petroleum Geology*, **20**, 901–910.

López-Gamundí and Rossello, E.A. (1998) Basin fill evolution and paleotectonic patterns along the Samfrau geosyncline: the Sauce Grande basin–Ventana foldbelt (Argentina) and Karoo basin-Cape foldbelt (South Africa) revisited. *Geologische Rundschau* **86,** 819-934.

Lowe, D.R. (1982) Sediment gravity flows: II. Depositional models with special reference to the deposits of high-density turbidity currents. *Journal of Sedimentary Petrology*, **52**, 279-297.

Lowe, D.R. and Guy, M. (2000) Slurry-flow deposits in the Britannia Formation (Lower Cretaceous), North Sea: a new perspective on the turbidity current and debris flow problem. *Sedimentology*, **47,** 31-70.

Luthi, S.M., Hodgson, D.M., Geel, C.R., Flint, S.S., Goedbloed, J.W., Drinkwater, N.J., Johanessen, E.P. (2006) Contribution of research borehole data to modelling fine-grained turbidite reservoir analogues, Permian Tanqua-Karoo basin floor fans (South Africa). *Petroleum Geology*, **12**, 175–190.

McCave, I.N. and Jones, K.P.N. (1988) Deposition of ungraded muds from high-density non-turbulent turbidity currents. *Nature,* **133**, 250-252.

Major, J.J. and Pierson, T.C. (1992) Debris Flow Rheology: Experimental analysis of fine-grained slurries. *Water Resources Research*, **28**, 841-857.

Martinsen, O. J., T. Lien, and R. G. Walker (2000) Upper Carboniferous deep water sediments, western Ireland: analogues for passive margin turbidite plays, in P. Weimer, R. M. Slatt, J. Coleman, N. C. Rossen, H. Nelson, A. H. Bouma, M. J. Styzen, and D. T. Lawrence, eds., Deep-water reservoirs of the world, Gulf Coast Section-SEPM Special Publication, p. 533-555.

McKay, M.P., Weislogel, A.L., Fildani, A., Brunt, R.L, Hodgson, D.M. and Flint, S.S. (2015) U–Pb zircon tuff geochronology from the Karoo Basin, South Africa: implications of zircon recycling on stratigraphic age controls. *International Geology Review*, **57**, 393–410.

Moiola, R.J. and Weiser, D. (1968) Textural parameters: An Evaluation. *Journal of Sedimentary Petrology*, **38**, 45-53.

Mohrig, D., and Buttles, J., 2007, Deep turbidity currents in shallow channels. *Geology*, v. 35, p. 155–158.

Morris, W.R., Scheilhing, M.H., Wickens, DeV., Bouma, A.H. (2000) Reservoir architecture of deepwater sandstones: examples from the Skoorsteenberg Formation, Tanqua Karoo Sub-Basin, South Africa. In: P. Weimer, R.M. Slatt, A.H. Bouma, and D.T. Lawrence, eds., Deep-water reservoirs of the world: Gulf Coast Section SEPM Foundation, Twentieth Annual Research Conference, p. 1010-1032.

Mutti, E. and Sonnino, M. (1981) Compensational cycles: a diagnostic feature of turbidite sandstone lobes. International Association of Sedimentologists 2nd European Meeting, Bologna, Italy, 120-123.

Parker, G., M. García, Y. Fukushima, and W. Yu (1987), Experiments on turbidity currents over an erodible bed. Journal of Hydraulic Research, **25**, 123–147.

Piper, D.J.W., and Normark, W.R. (1983) Turbidite depositional patterns and flow characteristics, Navy submarine fan, California Borderland. *Sedimentology*, **30**, 681–694.

Pirrie, D., Butcher, A.R., Power, M.R., Gottlieb, P., Miller, G.L. (2004), "Rapid quantitative mineral and phase analysis using automated scanning electron microscopy (QEMSCAN®); potential applications in forensic geoscience". In: Pye, K., Croft, D.J. (Eds.), Forensic Geoscience, Principles, Techniques and Applications, Vol. 232. Geological Society Special Publication, London, pp 23–136.

Pope, S.B. (2000) *Turbulent Flows.* Cambridge University Press, Cambridge, UK, 771 pp.

Porten, K.W., Kane, I.A., Warchoł, M.J. and Southern, S.J., in press. A sedimentological process-based approach to depositional reservoir quality of deep-marine sandstones: an example from the Springar Formation, north-western Vøring Basin, Norwegian Sea. *Journal of Sedimentary Research*.

Poyatos-More, M., Jones, G. D., Brunt, R., David M. Hodgson, Richard J. Wild, & Flint, S. (2016). Mud-dominated basin margin progradation: processes and implications. *Journal of Sedimentary Research*, **86**, 863-878.

Prélat, A. and Hodgson, D.M. (2013) *The full range of turbidite bed thickness patterns in submarine lobes: controls and implications***.** Journal of the Geological Society, **170**, 209-214.

Prélat, A., Hodgson, D.M. and Flint, S.S. (2009) Evolution, architecture and hierarchy of distributary deep-water deposits: a high-resolution outcrop investigation from the Permian Karoo Basin, South Africa. *Sedimentology*, 56, 2132-U25.

Pyles, D.R. and Jennette, D.C. (2009) Geometry and architectural associations of co-genetic debrite–turbidite beds in basin-margin strata, Carboniferous Ross Sandstone (Ireland): Applications to reservoirs located on the margins of structurally confined submarine fans. *Marine and Petroleum Geology*, **26,** 1974-1996.

Pysklywec, R.N. and Mitrovica, J.X. (1999) The role of subduction-induced subsidence in the evolution of the Karoo Basin. *The Journal of Geology,* **107**, 155-164.

Sequeiros, O.E. (2012) Estimating turbidity current conditions from channel morphology:A Froude number approach. *Journal of Geophysical Research*, **117**, C04003.

Smith, R.H.M. (1990) A review of stratigraphy and sedimentary environments of theKaroo basin of South Africa. *Journal of African Earth Sciences*, **10**, 117–137.

Southern, S.J., Patacci, M., Felletti, F. and McCaffrey, W.D. (2015) Influence of flow containment and substrate entrainment upon sandy hybrid event beds containing a co-genetic mud-clast-rich division. *Sedimentary Geology*, **321**. 105 - 122.

Southern, S.J., Kane, I.A., Warchoł, M.J., Porten, K.W. and McCaffrey, W.D. (2016) Hybrid event beds dominated by transitional-flow facies: Character, distribution and significance in the Maastrichtian Springar Formation, north-west Vøring Basin, Norwegian Sea. ***Sedimentology***, DOI: 10.1111/sed.12323

Spychala, Y.T, Hodgson, D.M., Stevenson, C.J. and Flint, S.S. (2016) Aggradational lobe fringes: The influence of subtle intrabasinal seabed topography on sediment gravity flow processes and lobe stacking patterns. *Sedimentology*. DOI: 10.1111/sed.12315

Spychala, Y.T., Hodgson, D.M., Prelat, A., Kane, I.A., Flint, S.S. and Mountney, N.P. (in press), Frontal and lateral submarine lobe fringes: Comparing sedimentary facies, architecture and flow processes. Journal of Sedimentary Research.

Stevenson, C.J., Jackson, C.A.L., Hodgson, D.M., Hubbard, S.M., and Eggenhuisen, J.T. 2015, Deep-water sediment bypass. *Journal of Sedimentary research*, 85, 1058-1081.

Sullivan, M.D., Jensen, G.N., Goulding, F.J., Jennette, D.C., Foreman, J.L. and Stern, D. (2000) Architectural analysis of deep-water outcrops: Implications for exploration and production of the Diana Sub-basin, western Gulf of Mexico, *in* P. Weimer, R.M. Slatt, A.H. Bouma, and D.T. Lawrence, eds., Deep-water reservoirs of the world: Gulf Coast Section SEPM Foundation, Twentieth Annual Research Conference, p. 1010-1032.

Sumner, E.J., Talling, P.J., and Amy, L.A. (2009) Deposits of flows transitional between turbidity current and debris flow. Geology, **37**, 991–994, doi:10.1130/G30059A.1.

Sylvester, Z. and Lowe, D.R. (2004) Textural trends in turbidites and slurry beds from the Oligocene flysch of the East Carpathians, Romania. Sedimentology, **51**, 945-972.

Talling, P.J., Amy, L.A., Wynn, R.B., Peakall, J. and Robinson, M. (2004) Beds comprising debrite sandwiched within co-genetic turbidite: origin and widespread occurrence in distal depositional environments. *Sedimentology*, **51,** 163-194.

Talling, P.J., Masson, D.G., Sumner, E.J. and **Malgesini, G.** (2012) Subaqueous sediment density flows: Depositional processes and deposit types. *Sedimentology*, **59**, 1937-2003.

Talling, P.J. (2013) Hybrid submarine flows comprising turbidity current and cohesive debris flow: Deposits, theoretical and experimental analyses, and generalized models: Geosphere, 9, 1-28.

Tankard A., Welsink H., Aukes P., Newton R., Stettler E. (2009) Tectonic evolution of the Cape and Karoo basins of South Africa. *Marine and Petroleum Geology*, **26**, 1379–1412. doi: 10.1016/j.marpetgeo.2009.01.022.

Terlaky, V., Arnott, R.W.C. (2014) Matrix-rich and associated matrix-poor sandstones: avulsion splays in slope and basin-floor strata. Sedimentology 61, 1175-1197. http://dx.doi.org/10.1111/sed.12096.

Twichell, D., Nelson, C.H., Kenyon, N. and Schwab, W. (2009) The Influence of External Processes on the Holocene Evolution of the Mississippi Fan, *in* B. Kneller, O.J. Martinsen, and B. McCaffrey, eds., External Controls on Deep-Water Depositional: SEPM Special Publication **92**, 145-157.

van der Werff, W. and Johnson, S. (2003a) High resolution stratigraphic analysis of turbidite system, Tanqua Karoo Basin, South Africa. *Marine and Petroleum Geology*, **20,** 45-69.

van der Werff, W. and Johnson, S.D. (2003b) Deep-sea fan pinch-out geometries and their relationship to fan architecture, Tanqua Karoo basin (South Africa). *International Journal of Earth Sciences*, **92,** 728-742.

Veevers, J.J., Cole, D.I. and Cowan, E.J. (1994) Souther Africa: Karoo Basin and Cape Fold Belt. In: *Permian-Triassic Pangean Basins and Foldbelts Along the Panthalassan Marginof Gondwanaland* (Eds J.J. Veevers and C.M. Powekk), **Memoir 184**, pp. 223-279. Geological Society of America.

Visser, J.N.J. (1997) Deglaciation sequences in the Permo-Carboniferous Karoo and Kalahari basins of the southern Africa: a toll in the analysis of cyclic glaciomarine basin fills. *Sedimentology,* **44**, 507-521.

Visser, J.N.J. and Prackelt, H.E. (1996) Subduction, mega-shear systems and Late Palaeozoic basin development in the African segment of Gondwana. *Geologische Rundschau,* **85**, 632-646.

Wan, Z. (1982) Bed Material Movement in Hyperconcentrated Flow. Institute of Hydrodynamics and Hydraulic Engineering, Technical University of Denmark, Lyngby, Series Paper, pp. 16–24.

Wickens, H.J. (1994) *Basin floor fan building turbidites of the southwestern Karoo Basin, Permian Ecca Group, South Africa*, University of Port Elizabeth, Unpublished, 233 pp.

Wild, R., Hodgson, D. and Flint, S. (2005) Architecture and stratigraphic evolution of multiple, vertically-stacked slope channel complexes, Tanqua depocentre, Karoo Basin, South Africa. In:

Submarine slope systems: processes and products (Eds D. Hodgson and S. Flint), **244**, pp. 89-111. The Geological Society of London, London.

Wild, R., Flint, S.S. and Hodgson, D.M. (2009) Stratigraphic evolution of the upper slope and shelf edge in the Karoo Basin, South Africa. *Basin Research*, **21,** 502-527.

Wintwerp, J.C., and van Kesteren, W.G.M. (2004). Introduction to the Physics of Cohesive Sediment in the Marine Environment: Oxford, U.K., Elsevier, Developments in Sedimentology 56, 559 p.

Wood, A. and Smith, A., J., (1958) The Sedimentation and Sedimentary History of the Aberystwyth Grits (Upper Llandoverian). *Quarterly Journal of the Geological Society*, **114,** 163-195.

Zarra, L., (2007) Chronostratigraphic Framework for the Wilcox Formation (Upper Paleocene-Lower Eocene) in the Deep-Water Gulf of Mexico: Biostratigraphy, Sequences, and Depositional Systems. In: Kennan, L., Pindell, J., and Rosen, N.C., eds., The Paleogene of the Gulf of Mexico and Caribbean Basins: Processes, Events, and Petroleum Systems: GCSSEPM Foundation 27th Annual Bob F. Perkins Research Conference, p. 81–145.

Zhiyao, S., Tingting, W., Fumin, X. and Ruijie, L. (2008). A simple formula for predicting settling velocity of sediment particles. *Water Science and Engineering Journal*, **1**, 37– 43.

Table & Figure Captions

Table 1. Mineralogical composition of samples analysed using QEMSCAN. Heavy outlines mark individual beds, which are classified here as hybrid beds (HB), turbidites (TURB) and thick amalgamated sandstone – see text (AMAL), the lowermost and uppermost samples for each bed are marked (-base and -top respectively).

Table 2. Grain fabric data. Heavy outlines mark individual beds, which are classified here as HB (hybrid bed), TURB (turbidite) and AMAL (thick amalgamated sandstone – see text).

Figure 1. A) Aerial image of part of South Africa, highlighting the location of the Tanqua Depocentre, approximately 90 km northwest of the town of Laingsburg. B) Outline of Fan 3 in the Tanqua Depocentre (from Hodgson et al., 2006); the field area is boxed and expanded in 'D' and 'E'. Blue arrows show the general palaeoflow trends. C) Aerial image of the field area, illustrating the outcrop continuity of the near horizontal bedding surfaces, and the location of the measured sections. D) Schematic stratigraphic log of the Permian to earliest Triassic deep-marine to fluvial fill of the Tanqua depocentre (modified from Wild et al., 2005). E) Simple geological map illustrating the position of Fan 3 (bold line) and stratigraphic packages between fan tops. At this scale the fan tops are the only mappable surfaces, as the fans tend to weather into steep outcrop faces, whereas the finer-grained inter-fans form gentler slopes. The sandy part of Fan 2 has pinched out in this area (pinching out to the north), and is beneath the resolution of this map; Fan 1 has pinched out. The uppermost package, i.e., 'Top Unit 5 and younger', is predominantly the Kookfontein Fm.

Figure 2. A) Correlation panel of 1:20 outcrop logs SK1-20; positions of 1:2 logs are shown alongside the relevant log. The correlations are based on walking out key stratigraphic surfaces, the lobes stack to form a lobe complex (Fan 3). Note that lobes 1 and 3 have pinched out in this position. The outcrop panel (B) shows the general character and exposure of the distal parts of Fan 3. C, D and E illustrate the general outcrop character at the positions of logs SK11, SK9 and SK7 respectively. The yellow and grey colouring gives a general indication of the sandstone (yellow) and mudstone (grey) distribution. Palaeoflow is to the north, approximately right to left in the image.

Figure 3. (A) Correlation panel of logged sections from behind outcrop boreholes, spanning Fan 3 from the proximal channel-dominated part (Ongeluks River outcrops), to the channel-lobe transition and across the lobe to the distal parts studied here (e.g., Boreholes NB2-NS1). Note that the environments indicated are at the point of the arrows, not spanning the entire fan at that location. Correlations are tentative owing to the complex nature of compensational lobe stacking patterns and based on finer-grained intervals subdividing the sandstone rich element, following Prélat et al., 2009. A clear facies trend is observed across the lobe complex, illustrated by the plan view image (B).

Figure 4. Sedimentary logs through Fan 3, positions shown in Figure 1.

Figure 5. Detailed sedimentary logs from Fan 3, positions shown in Figure 1.

Fig. 6. Representative turbidite facies. A) Thick bedded turbidite with a sharp base, weak normal grading and with a clast-rich upper part; clasts are partly disaggregated generating clay-rich patches within the sandstone. B) Erosional bed bases typically plane out on mudstones and cut downwards in a stepwise manner through thin-bedded intervals, occasionally with contemporaneous lateral injection. C) Erosional step at base of medium-bedded sandstone which is loaded into underlying thin-bedded silty turbidites. D) Thin-bedded very-fine-grained low-density turbidites. E) Rippled bed top to low density turbidite. F) Plant imprints in an intra-bed division.

Fig. 7. Representative hybrid bed photographs (‘B’ and ‘T’ symbols indicate base and top of beds). A) Bed showing intense interaction with the substrate and muddy upper part, these are typical in medial lobe settings. B & C) Hybrid beds with thick laminar/ high concentration flow deposits in their upper parts; these are typical in medial to distal settings. D) Hybrid beds with large rafts of siltstone and mudstone. E & F) Thin hybrid beds characteristic of the distal facies, with thin relatively clean sands at bed bases and overlying layers of varying mud content.

Figure 8. Photographs from cores of representative facies. A) Thin-bedded low-density turbidites; B) Thinly-interbedded low-density turbidites dominated by planar-lamination (i), small-scale load and flame structures (ii), and ripple-cross lamination (iii). C) Silty low-density turbidites graded from medium silt (i) to very-fine silt (ii). D) Turbidite with loading and injection of the substrate at the base. The upper part of the bed is truncated (i). E) Detail of loading and deformation at the base of a turbidite. F) Muddy sandstone truncated by an erosion surface overlain by claystone (bypass surface) and overlain by an argillaceous sandstone. G) Small injectite extending from a bed top. H) Dewatering pillars in the upper part of a hybrid bed, (ii) large mudstone clasts. I) Thick debrite with cleaner sandstone ‘balls’ and injections in an overall muddy sand matrix.

Fig. 9. Quartz-feldspar-lithics (QFL) plot for samples subdivided into ‘turbidites’ and ‘hybrid beds. Turbidites fall entirely within the lithic arkose class, whilst hybrid beds span the lithic arkose and feldspathic litharenite classes. Ternary plot from Folk (1974).

Figure 10. Mineral maps from thin-sections, based on chemical composition data from QEMSCAN. A-F show samples SK7A, B, C, D, H and I respectively. SK7A-D are interpreted as hybrid beds whilst SK7H and SK7I are interpreted as turbidites (see table 1).

Figure 11. Representative thin-section photomicrographs. A) Sample SK7B: clay-rich sample from the middle part of a hybrid bed. Note the organic fragments and porosity (blue) due to dissolution of framework minerals (probably feldspar). B) Sample SK7C: from the middle division of a hybrid bed, this clay-rich sandstone has a strong bed-parallel grain fabric, with aligned claystone and organic clasts. C) Sample SK7D: Sample from a thick muddy division within a hybrid bed, note the strong grain fabric with lens of coarser-grained sediment in the centre of the image. The sample lacks visible porosity. D) Sample SK7E: Mixed 'swirled' fabric of relatively finer- and coarser-grained lenses. This sample is from a lighter coloured band in a hybrid bed. The large rounded clast is a claystone. Note the porosity due to grain dissolution. E) Sample SK7H: This sample is from a tractional sandstone with weak plane-parallel lamination, which has a much lower mud content than the previous examples, and an alignment of quartz and feldspar grains along laminae. F) Sample SH7I. This sample is from the very-thick bed which caps Fan 3 at the SK7 locality. It does not appear to have a strong grain fabric in thin-section and in outcrop lacks obvious tractional structure. The visible porosity is most-likely related to weathering processes and fracturing around coarser grains.

Figure 12. Thin-section photomicrographs in plane polarized light, from an argillaceous sandstone division of a hybrid bed (Sample SK7A, Log SK7. A) Illustration of the very low degree of porosity in these rocks (blue colors indicate open pore spaces). B) The porosity that is present is predominantly secondary, mostly through grain dissolution of feldspars; this example shows remnant grain material preserved. C&D) Sample SK7F, interpreted as a hybrid bed. Thin section micrographs in plane polarized light (C) and with crossed polars (D). These images clearly show the abundant rock fragments which are common in all of the sampled rocks. Some fragments appear to be of carbonate rocks (I), although discrimination from altered plagioclase can be difficult, whilst others are composed of multiple minerals (II); calcite is recorded in the QEMSCAN mineralogical analysis for this sample.

Figure 13. Summary diagrams illustrating grain-size trends, sorting, mineralogy and grain fabric for representative examples of hybrid beds (A, B, C) and one turbidite (D). Note that the straight lines between data points are for illustration only and do not indicate that data points can necessarily be extrapolated.

Figure 14. Grain-size distribution curves for individual hybrid and turbidite beds. Whilst the grain size curves are largely distinctive for the different flow types (summarised in Fig. 15), SK2 although

described as a hybrid bed has much the same character as a turbidite, albeit slightly enriched in coarser grains and with a more clay rich top (see Table 1).

Figure 15. Representative grains-size distribution for deposits described as A) turbidites and B) hybrid beds. Turbidites are characterised by positively (fine) skewed lower bed divisions, and typically symmetrical upper divisions; in contrast, hybrid beds are characterised by negative (coarse) skewed lower divisions and symmetrical to coarse upper divisions.

Figure 16. Flow parameters along lobe length for a scenario where channel width is 250 m; channel depth and initial flow thickness are 13 m and 17 m respectively; flow concentration is 5%; slope is $1.5*10^{-3}$; lobe width is 15 km; lobe length is 25km. (A) Flow width increases linearly over the lobe length from the channel width at the lobe apex to the full lobe width. Flow thickness decreases rapidly proximally, and more slowly distally. (B) Average velocity (left y-axis) and bed-shear velocity (right y-axis). Plots overlap because the drag coefficient has been used to normalise the right y-axis according to Eq. (4). (C) Suspension capacity parameter Γ is much larger than 1 at the lobe apex, indicating undersaturated near-bed conditions, reaches the threshold value of $\Gamma = 1$ 21 km downstream of the lobe apex, and $\Gamma < 1$, leading to turbulence suppression, downstream of 21 km.

Figure 17. The sensitivity of the downstream evolution of Γ to different estimations for inlet concentration and slope. (A) Sediment concentrations of 10%, 5%, 1%, and 0.5%; for a given slope, the distance to flow transformation increases with increasing sediment concentration. (B) Slope gradients of $5.0*10^{-3}$, $2.5*10^{-3}$, $1.5*10^{-3}$, $1*10^{-3}$, and $5.0*10^{-4}$; for a given concentration, the distance to flow transformation increases with increasing slope.

Figure 18. A) Schematic perspective/plan view of Fans 3. The distribution of hybrid beds is illustrated with schematic logs (see 'B'), but note that the fan fringe is not limited to hybrid beds, low-density turbidites are also common. At t0, in the trunk channels, flows are undersaturated with respect to the flow suspension capacity ($\Gamma > 1$) and strongly erosional; high density turbidites are amalgamated and can be mudstone-clast rich. B) Summary diagram of flow evolution and deposit type for flows in the fringe area which start out, at t1, fully turbulent and well mixed and undersaturated ($\Gamma > 1$), capable of eroding and entraining substrate. As flows decelerate from the channel-lobe transition (t2), shear stress exerted on the bed decreases, leaving substrate interaction preserved and resultant deposits clast and mud rich. Further deceleration and enrichment in cohesive

and fine grained material (t3) results in the concentration profile becoming increasingly stratified and, when flows drop below the critical value of Γ=1 they are oversaturated and suspension capacity is lost. A dense lower layer forms, which continues to move downstream owing to its high water content (due to clays and very fine silts), grains are supported by yield strength but coarser grains settle resulting in a relatively well sorted sand fraction within a mud-rich matrix. Overlying layers are muddier and less well sorted. The formation of this high concentration lower boundary layer flow inhibits the transmission of turbulent kinetic energy into the upper part of the flow and turbulence is rapidly dissipated (t4).

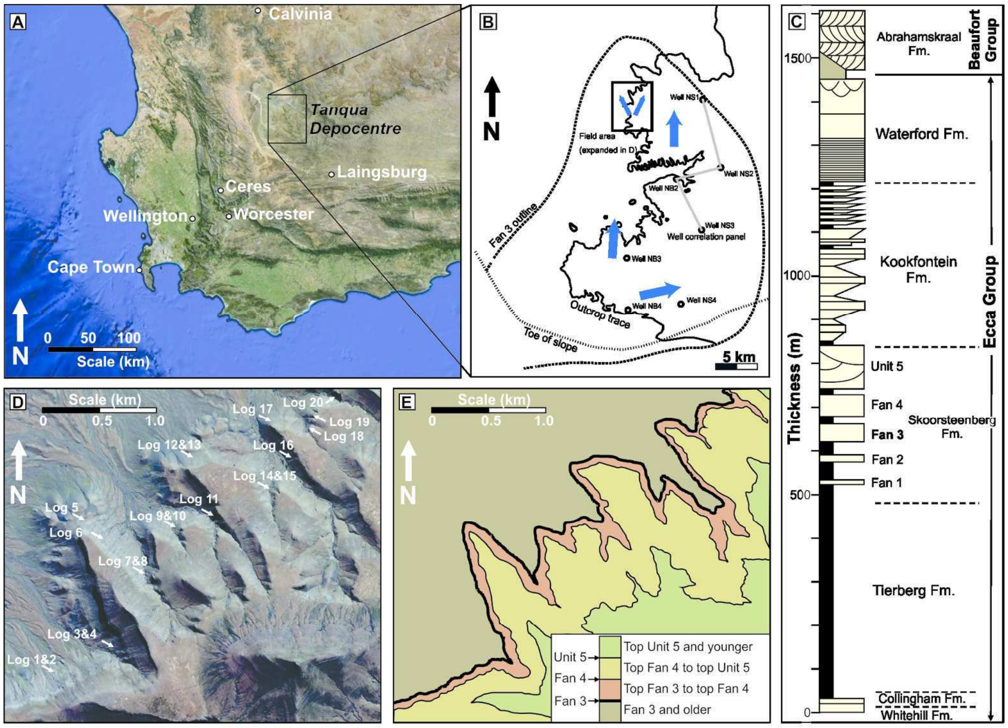

Figure 1. A) Aerial image of part of South Africa, highlighting the location of the Tanqua Depocentre, approximately 90 km northwest of the town of Laingsburg. B) Outline of Fan 3 in the Tanqua Depocentre (from Hodgson et al., 2006); the field area is boxed and expanded in 'D' and 'E'. Blue arrows show the general palaeoflow trends. C) Aerial image of the field area, illustrating the outcrop continuity of the near horizontal bedding surfaces, and the location of the measured sections. D) Schematic stratigraphic log of the Permian to earliest Triassic deep-marine to fluvial fill of the Tanqua depocentre (modified from Wild et al., 2005). E) Simple geological map illustrating the position of Fan 3 (bold line) and stratigraphic packages between fan tops. At this scale the fan tops are the only mappable surfaces, as the fans tend to weather into steep outcrop faces, whereas the finer-grained inter-fans form gentler slopes. The sandy part of Fan 2 has pinched out in this area (pinching out to the north), and is beneath the resolution of this map; Fan 1 has pinched out. The uppermost package, i.e., 'Top Unit 5 and younger', is predominantly the Kookfontein Fm.

170x123mm (300 x 300 DPI)

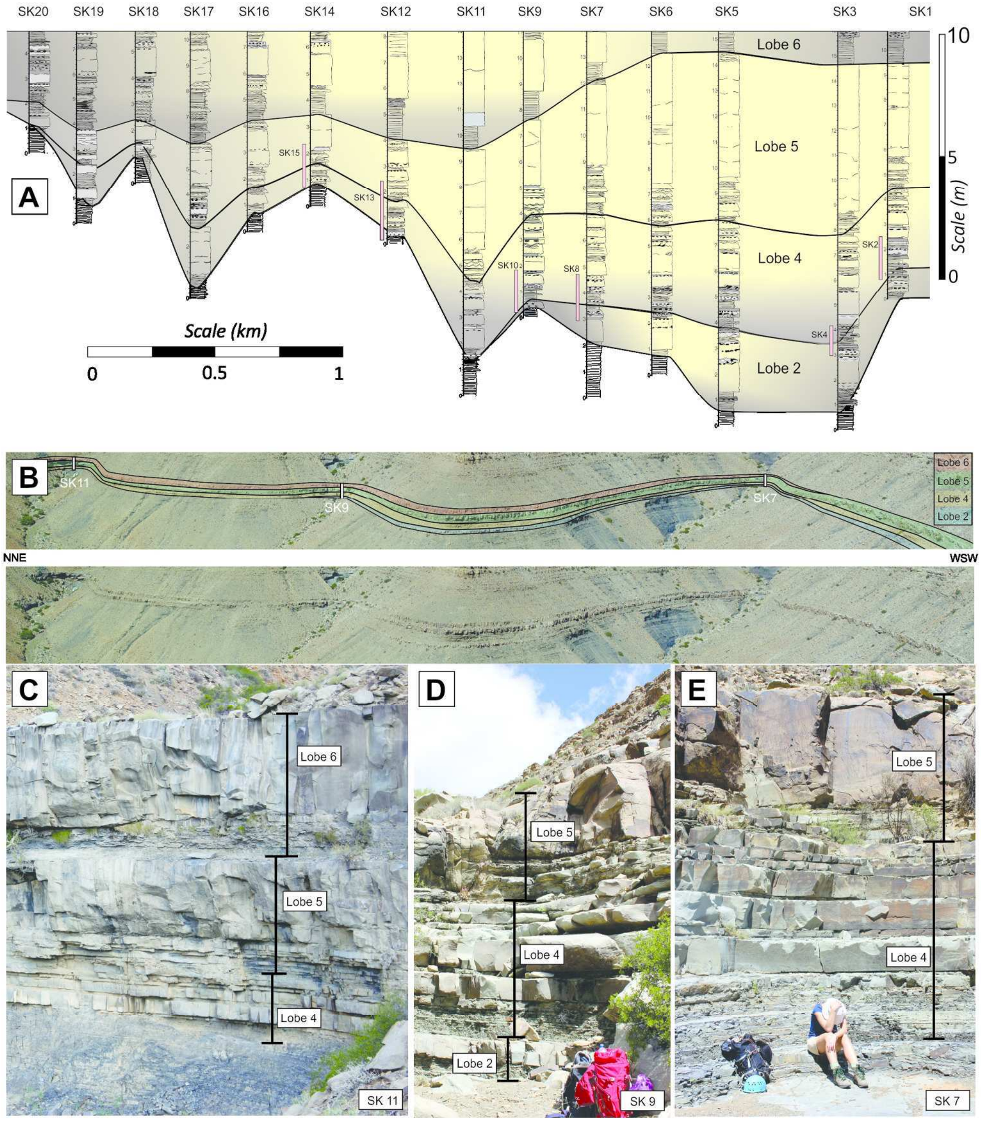

Figure 2. A) Correlation panel of 1:20 outcrop logs SK1-20; positions of 1:2 logs are shown alongside the relevant log. The correlations are based on walking out key stratigraphic surfaces, the lobes stack to form a lobe complex (Fan 3). Note that lobes 1 and 3 have pinched out in this position. The outcrop panel (B) shows the general character and exposure of the distal parts of Fan 3. C, D and E illustrate the general outcrop character at the positions of logs SK11, SK9 and SK7 respectively. The yellow and grey colouring gives a general indication of the sandstone (yellow) and mudstone (grey) distribution. Palaeoflow is to the north, approximately right to left in the image.

196x223mm (300 x 300 DPI)

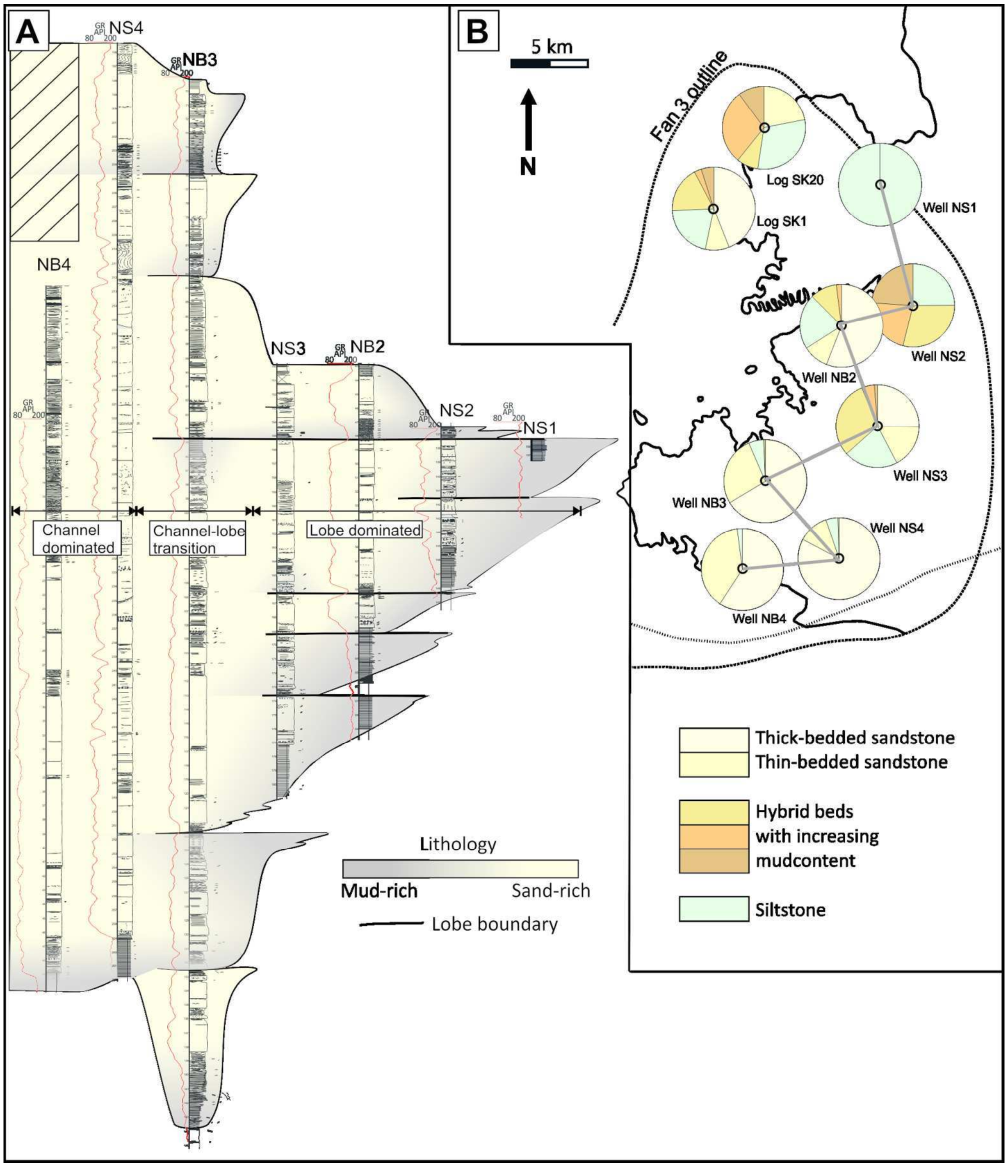

Figure 3. (A) Correlation panel of logged sections from behind outcrop boreholes, spanning Fan 3 from the proximal channel-dominated part (Ongeluks River outcrops), to the channel-lobe transition and across the lobe to the distal parts studied here (e.g., Boreholes NB2-NS1). Note that the environments indicated are at the point of the arrows, not spanning the entire fan at that location. Correlations are tentative owing to the complex nature of compensational lobe stacking patterns and based on finer-grained intervals subdividing the sandstone rich element, following Prélat et al., 2009. A clear facies trend is observed across the lobe complex, illustrated by the plan view image (B).

170x197mm (300 x 300 DPI)

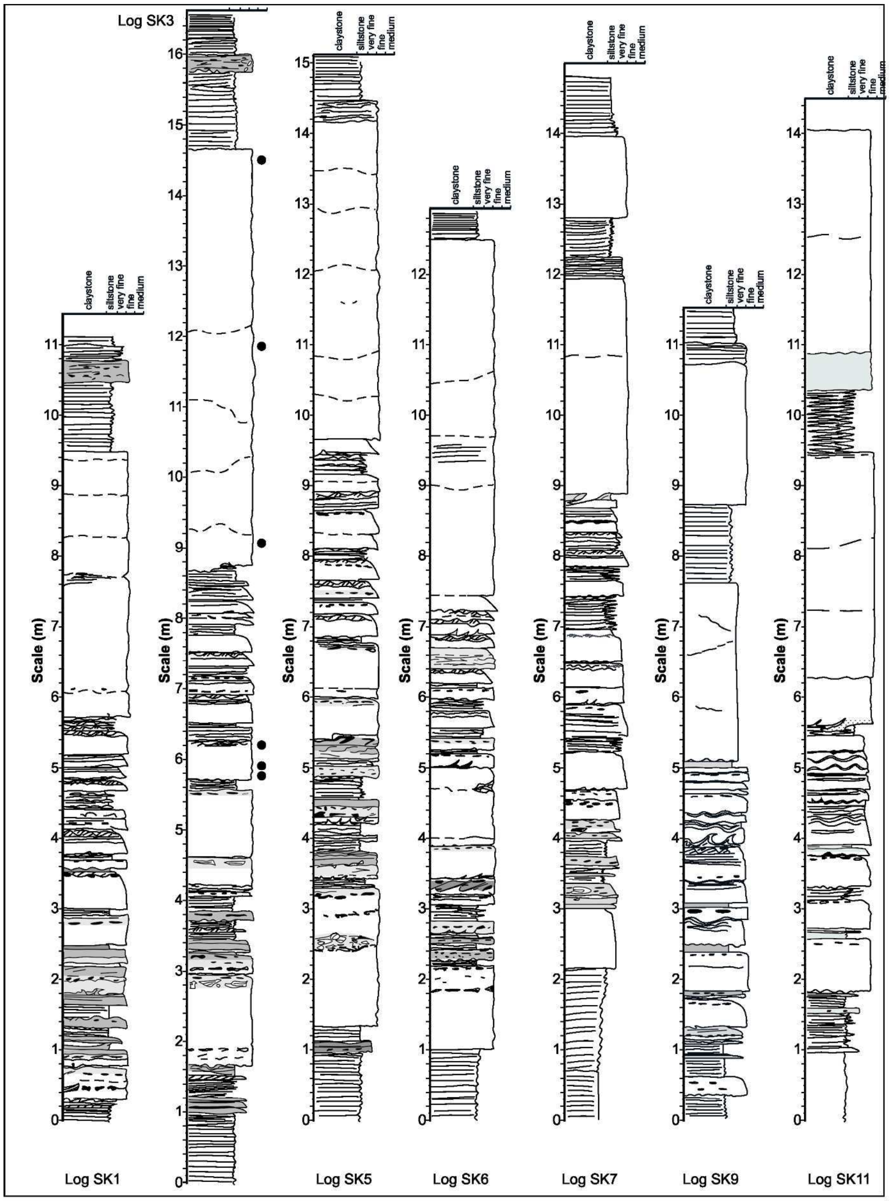

Figure 4. Sedimentary logs through Fan 3, positions shown in Figure 1.

173x231mm (300 x 300 DPI)

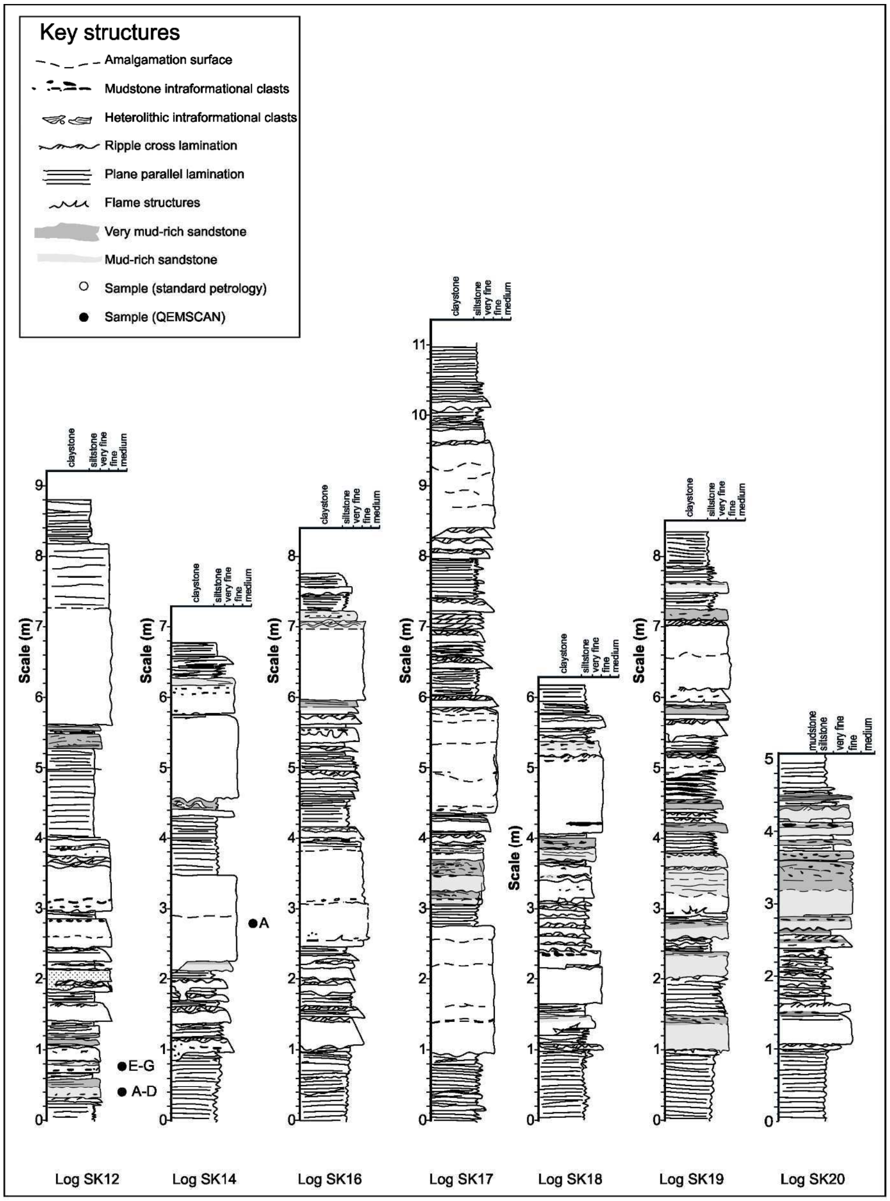

Figure 4. Sedimentary logs through Fan 3, positions shown in Figure 1.

170x231mm (300 x 300 DPI)

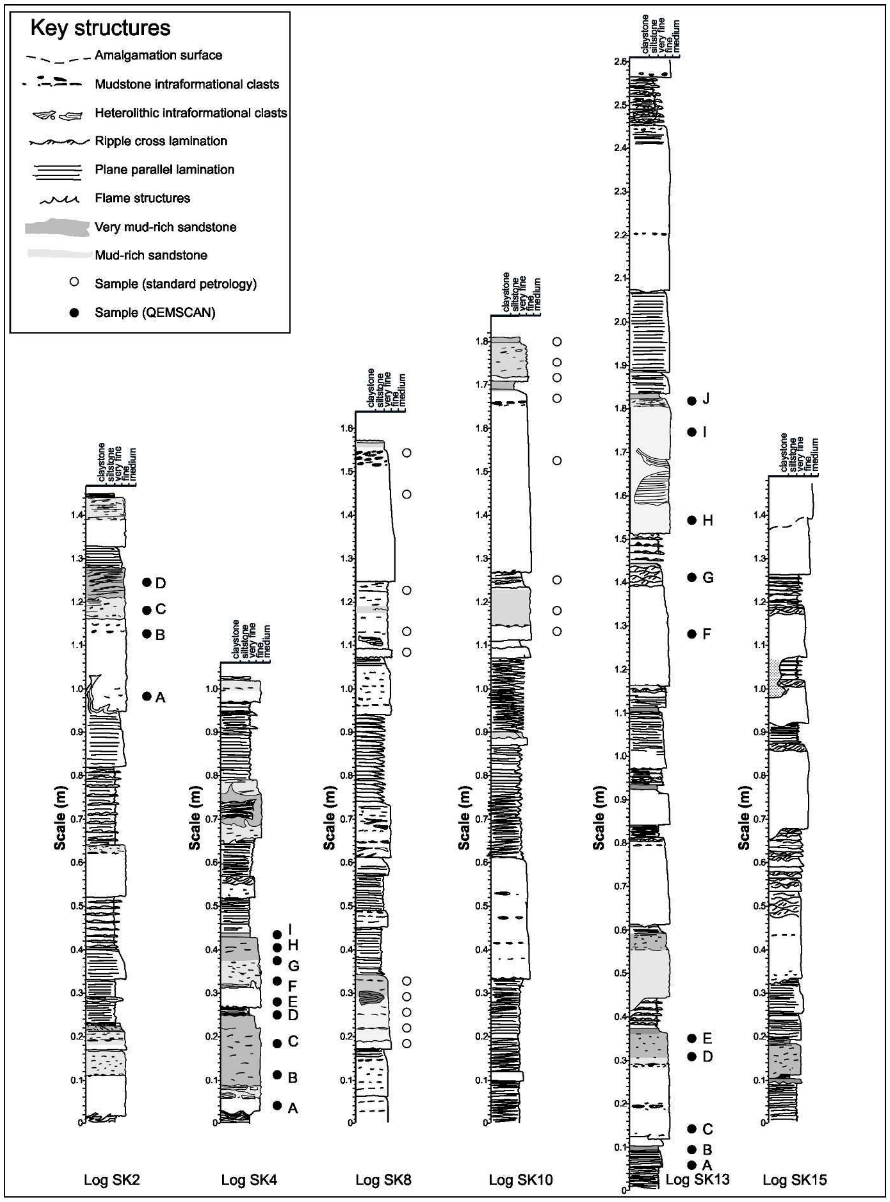

Figure 5. Detailed sedimentary logs from Fan 3, positions shown in Figure 1.

170x231mm (300 x 300 DPI)

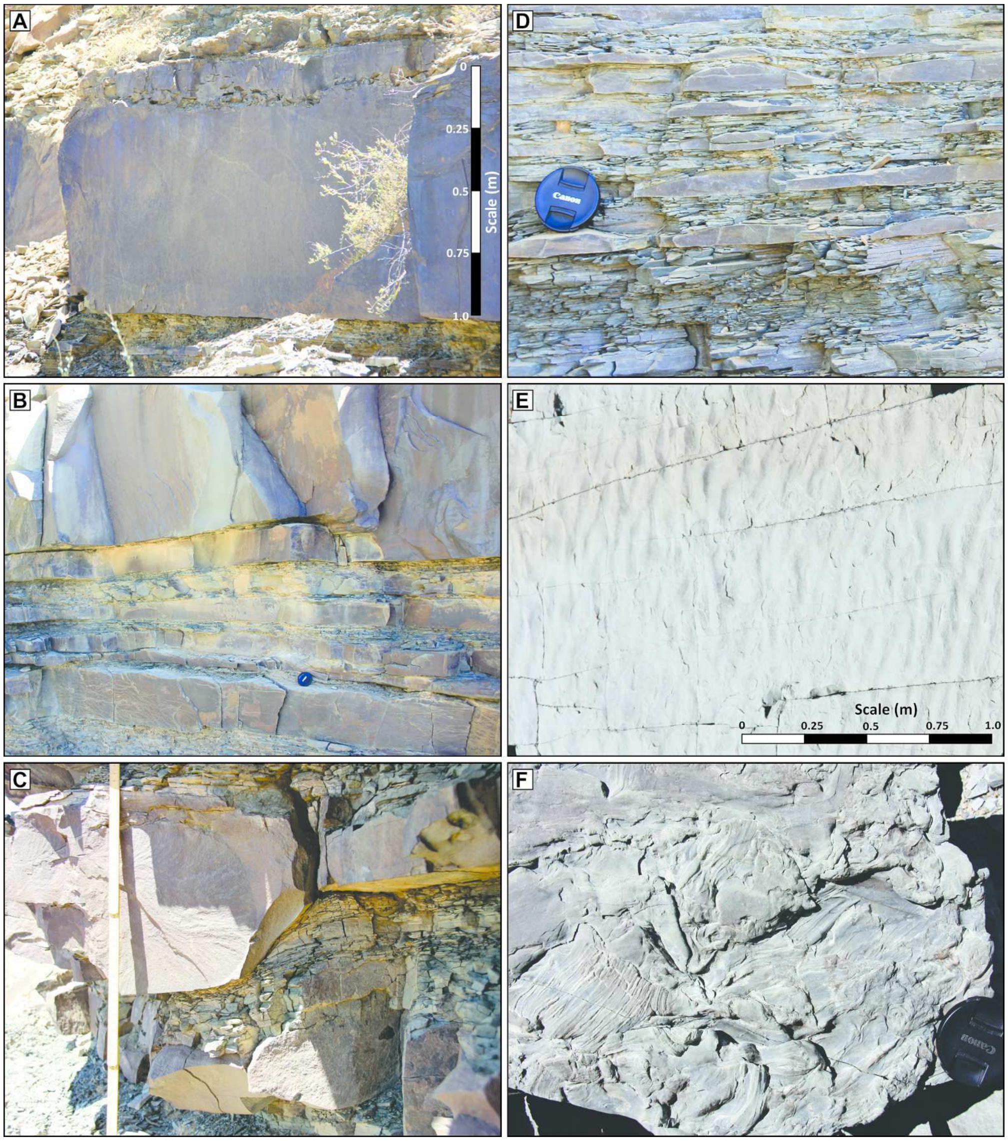

Fig. 6. Representative turbidite facies. A) Thick bedded turbidite with a sharp base, weak normal grading and with a clast-rich upper part; clasts are partly disaggregated generating clay-rich patches within the sandstone. B) Erosional bed bases typically plane out on mudstones and cut downwards in a stepwise manner through thin-bedded intervals, occasionally with contemporaneous lateral injection. C) Erosional step at base of medium-bedded sandstone which is loaded into underlying thin-bedded silty turbidites. D) Thin-bedded very-fine-grained low-density turbidites. E) Rippled bed top to low density turbidite. F) Plant imprints in an intra-bed division.

170x192mm (300 x 300 DPI)

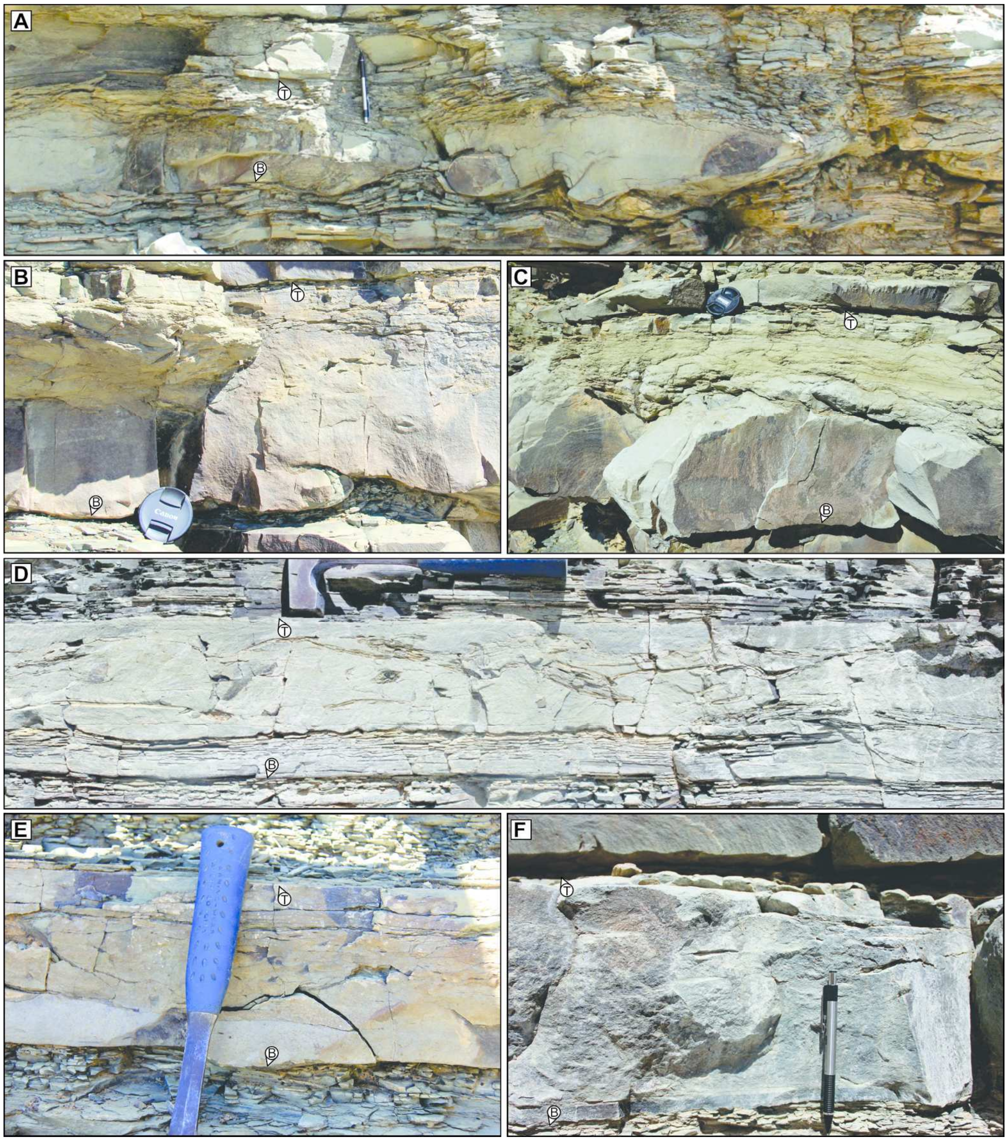

Fig. 7. Representative hybrid bed photographs ('B' and 'T' symbols indicate base and top of beds). A) Bed showing intense interaction with the substrate and muddy upper part, these are typical in medial lobe settings. B & C) Hybrid beds with thick laminar/ high concentration flow deposits in their upper parts; these are typical in medial to distal settings. D) Hybrid beds with large rafts of siltstone and mudstone. E & F) Thin hybrid beds characteristic of the distal facies, with thin relatively clean sands at bed bases and overlying layers of varying mud content.

170x192mm (300 x 300 DPI)

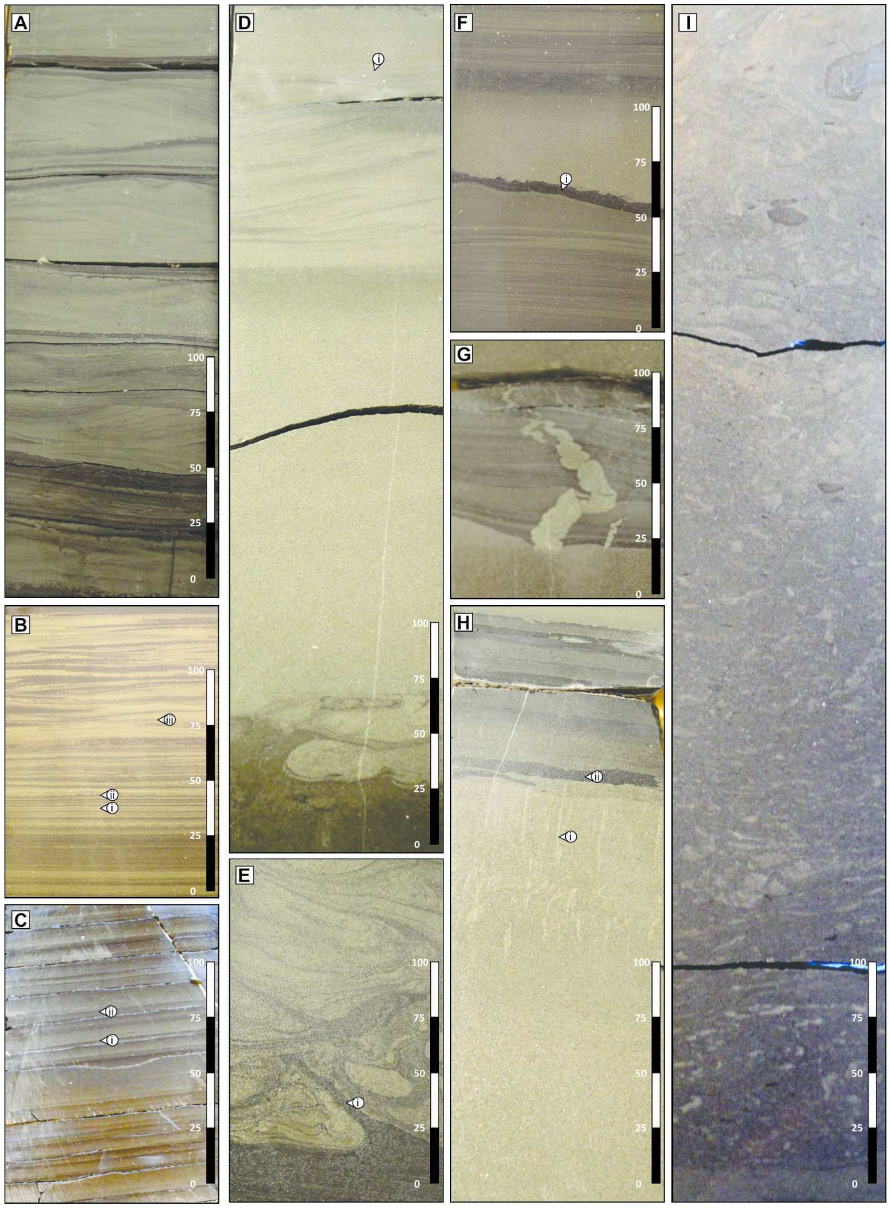

Figure 8. Photographs from cores of representative facies. A) Thin-bedded low-density turbidites; B) Thinly-interbedded low-density turbidites dominated by planar-lamination (i), small-scale load and flame structures (ii), and ripple-cross lamination (iii). C) Silty low-density turbidites graded from medium silt (i) to very-fine silt (ii). D) Turbidite with loading and injection of the substrate at the base. The upper part of the bed is truncated (i). E) Detail of loading and deformation at the base of a turbidite. F) Muddy sandstone truncated by an erosion surface overlain by claystone (bypass surface) and overlain by an argillaceous sandstone. G) Small injectite extending from a bed top. H) Dewatering pillars in the upper part of a hybrid bed, (ii) large mudstone clasts. I) Thick debrite with cleaner sandstone 'balls' and injections in an overall muddy sand matrix.

169x229mm (300 x 300 DPI)

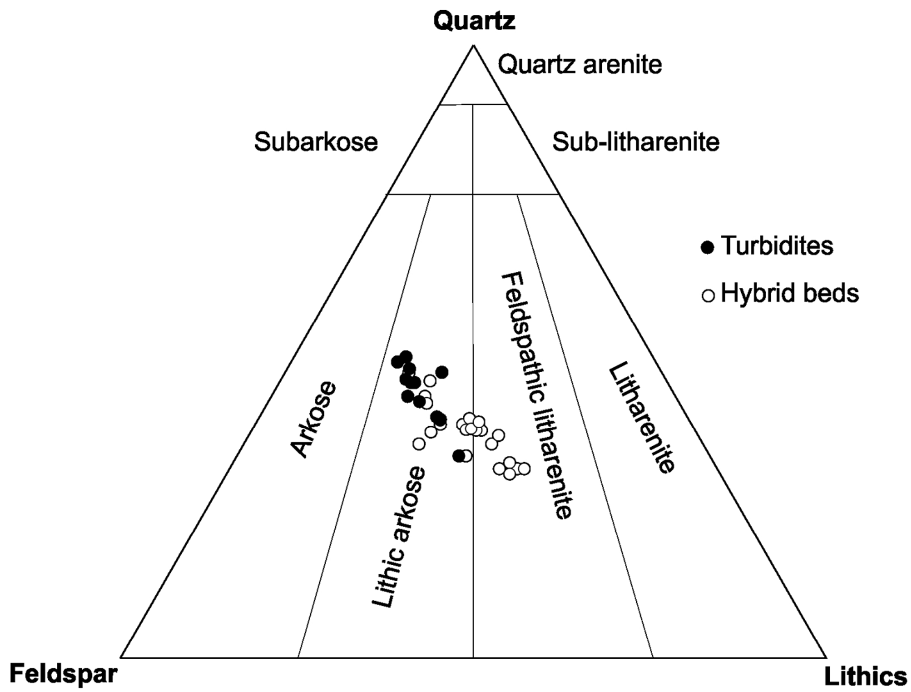

Fig. 9. Quartz-feldspar-lithics (QFL) plot for samples subdivided into 'turbidites' and 'hybrid beds. Turbidites fall entirely within the lithic arkose class, whilst hybrid beds span the lithic arkose and feldspathic litharenite classes. Ternary plot from Folk (1974).

149x110mm (300 x 300 DPI)

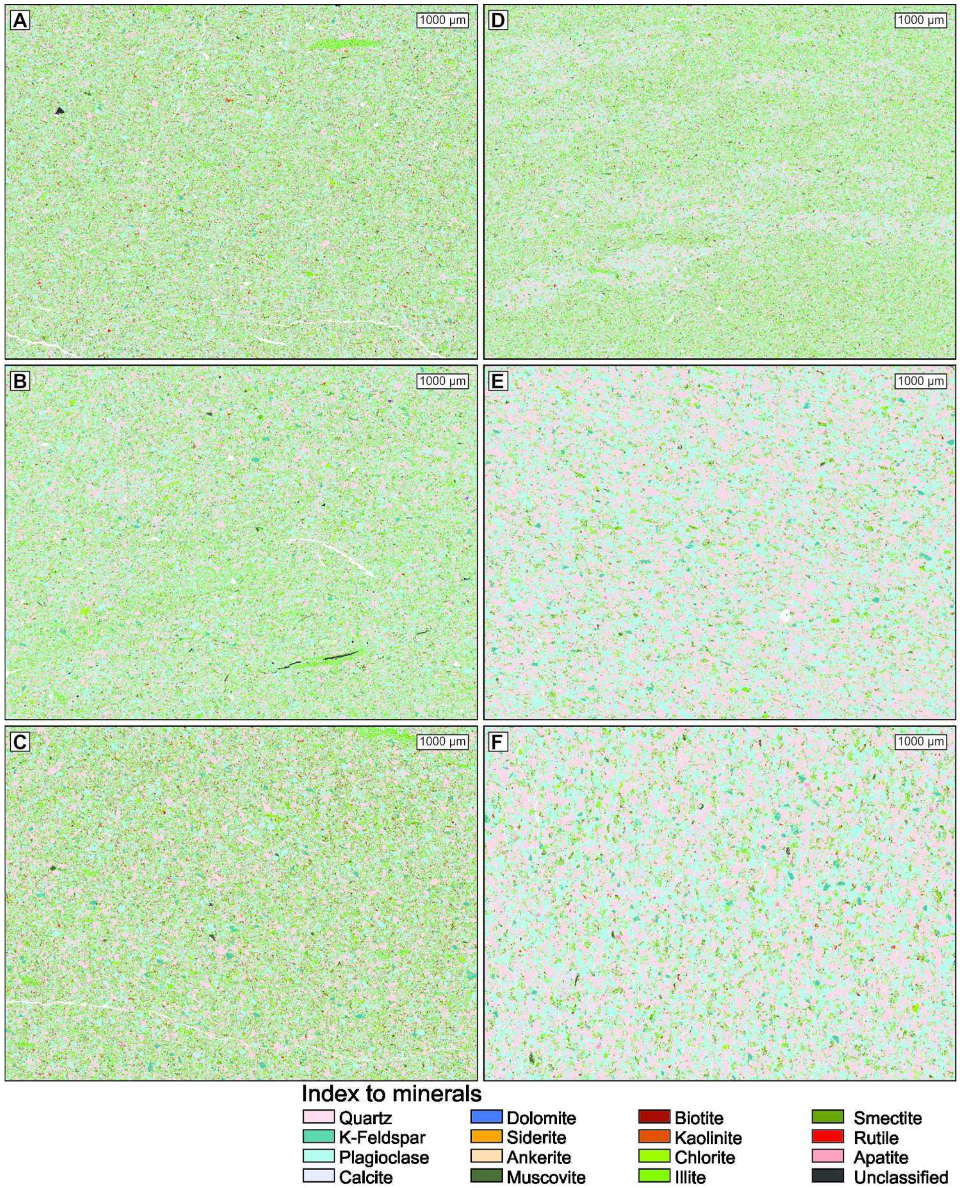

Figure 10. Mineral maps from thin-sections, based on chemical composition data from QEMSCAN. A-F show samples SK7A, B, C, D, H and I respectively. SK7A-D are interpreted as hybrid beds whilst SK7H and SK7I are interpreted as turbidites (see table 1).

170x214mm (300 x 300 DPI)

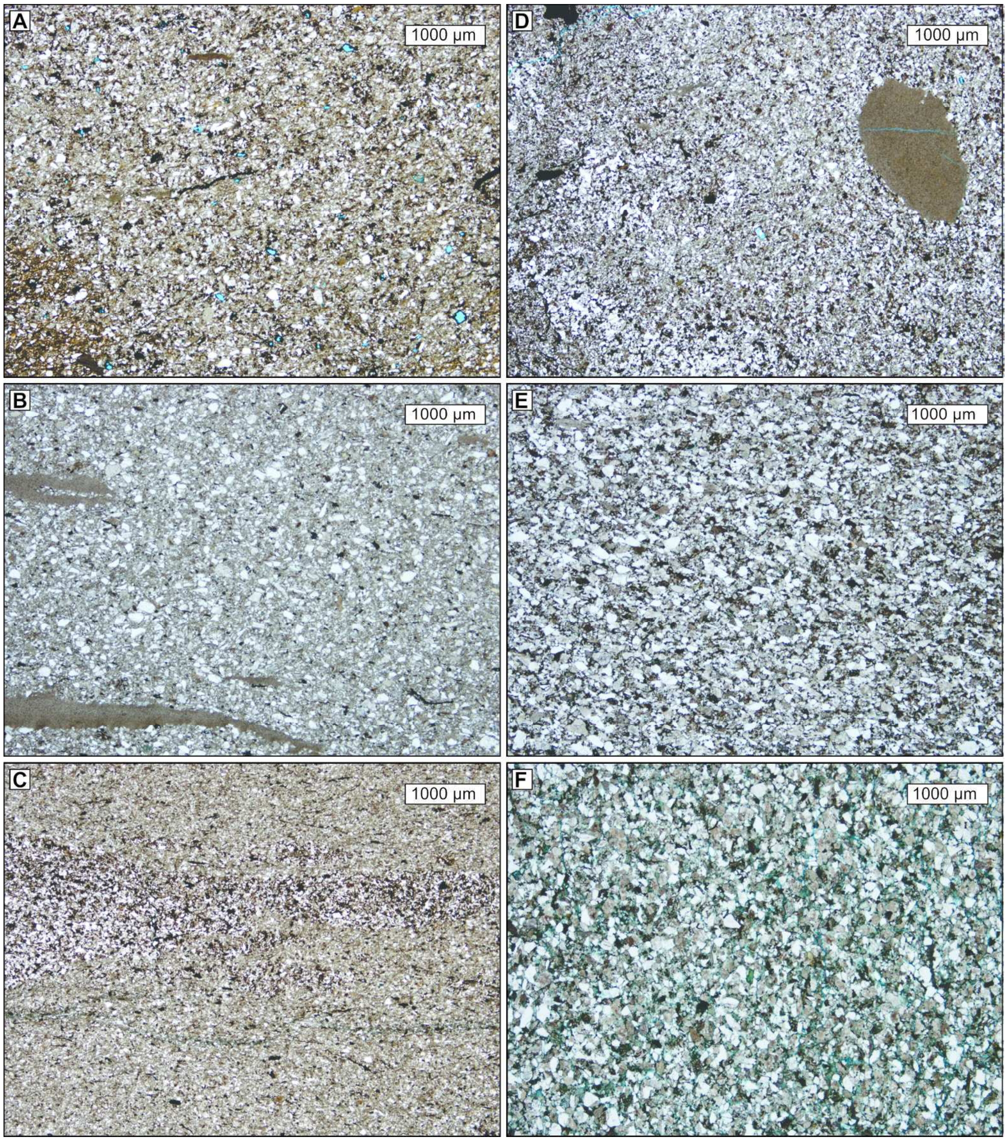

Figure 11. Representative thin-section photomicrographs. A) Sample SK7B: clay-rich sample from the middle part of a hybrid bed. Note the organic fragments and porosity (blue) due to dissolution of framework minerals (probably feldspar). B) Sample SK7C: from the middle division of a hybrid bed, this clay-rich sandstone has a strong bed-parallel grain fabric, with aligned claystone and organic clasts. C) Sample SK7D: Sample from a thick muddy division within a hybrid bed, note the strong grain fabric with lens of coarser-grained sediment in the centre of the image. The sample lacks visible porosity. D) Sample SK7E: Mixed 'swirled' fabric of relatively finer- and coarser-grained lenses. This sample is from a lighter coloured band in a hybrid bed. The large rounded clast is a claystone. Note the porosity due to grain dissolution. E) Sample SK7H: This sample is from a tractional sandstone with weak plane-parallel lamination, which has a much lower mud content than the previous examples, and an alignment of quartz and feldspar grains along laminae. F) Sample SH7I. This sample is from the very-thick bed which caps Fan 3 at the SK7 locality. It does not appear to have a strong grain fabric in thin-section and in outcrop lacks obvious tractional structure. The visible porosity is most-likely related to weathering processes and fracturing around coarser grains.

170x192mm (300 x 300 DPI)

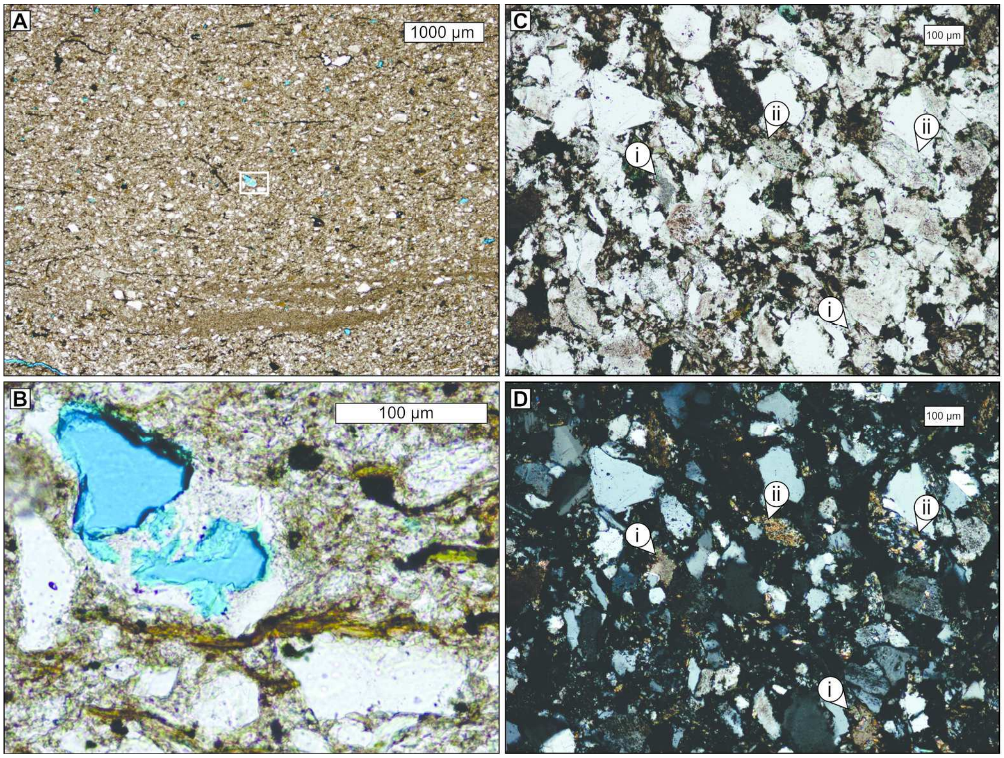

Figure 12. Thin-section photomicrographs in plane polarized light, from an argillaceous sandstone division of a hybrid bed (Sample SK7A, Log SK7. A) Illustration of the very low degree of porosity in these rocks (blue colors indicate open pore spaces). B) The porosity that is present is predominantly secondary, mostly through grain dissolution of feldspars; this example shows remnant grain material preserved. C&D) Sample SK7F, interpreted as a hybrid bed. Thin section micrographs in plane polarized light (C) and with crossed polars (D). These images clearly show the abundant rock fragments which are common in all of the sampled rocks. Some fragments appear to be of carbonate rocks (I), although discrimination from altered plagioclase can be difficult, whilst others are composed of multiple minerals (II); calcite is recorded in the QEMSCAN mineralogical analysis for this sample.

170x128mm (300 x 300 DPI)

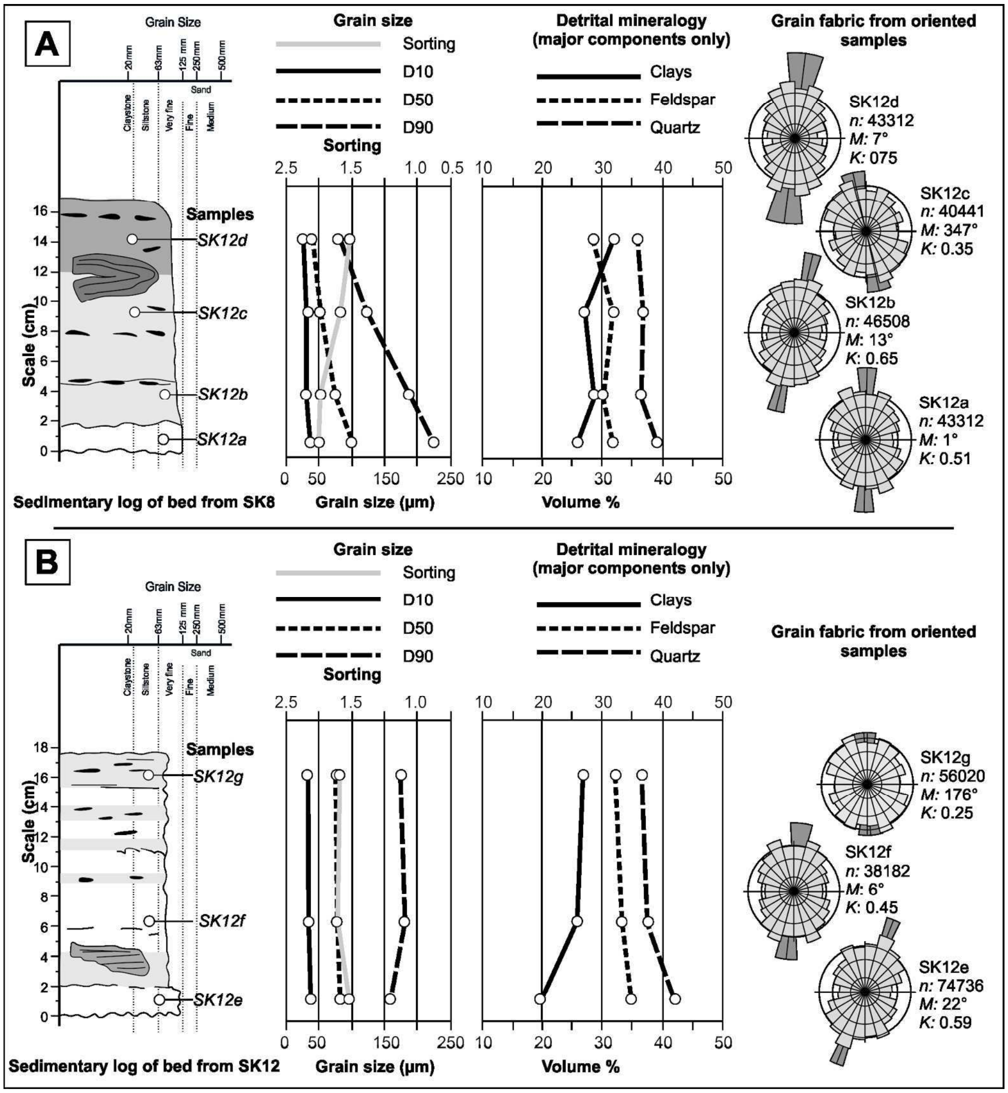

Figure 13. Summary diagrams illustrating grain-size trends, sorting, mineralogy and grain fabric for representative examples of hybrid beds (A, B, C) and one turbidite (D). Note that the straight lines between data points are for illustration only and do not indicate that data points can necessarily be extrapolated.

170x184mm (300 x 300 DPI)

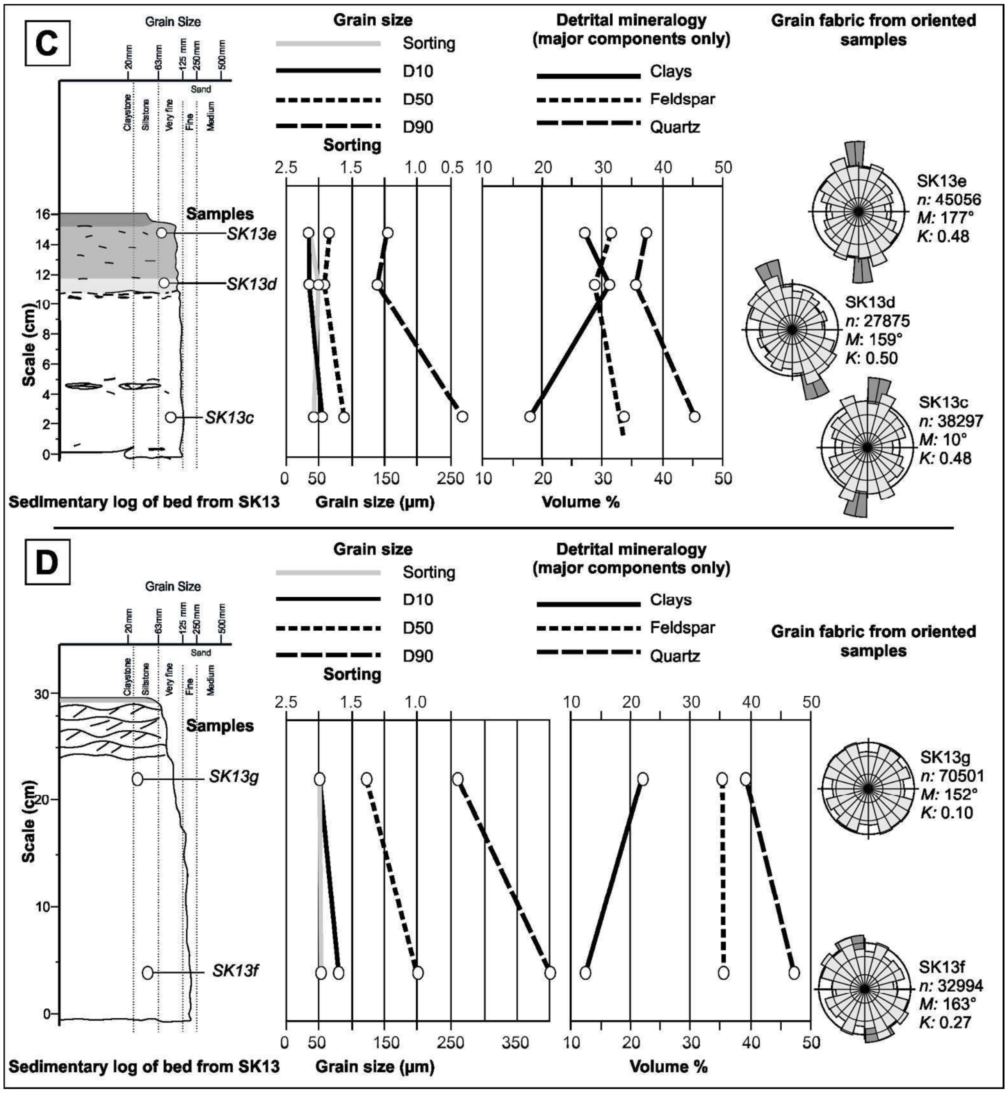

Figure 13. Summary diagrams illustrating grain size trends, sorting, mineralogy and grain fabric for representative examples of hybrid beds (A, B, C) and one turbidite (D). Note that the straight lines between data points are for illustration only and do not indicate that data points can necessarily be extrapolated.

170x184mm (300 x 300 DPI)

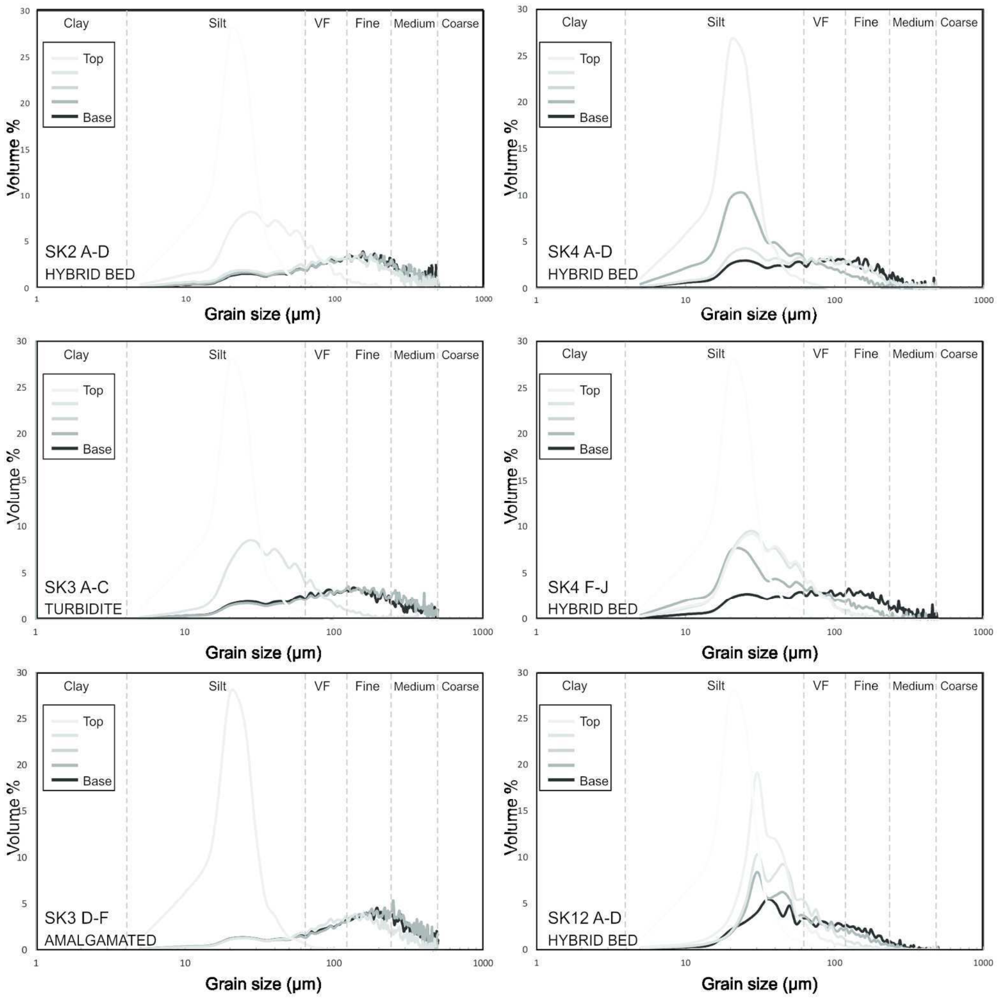

Figure 14. Grain size distribution curves for individual hybrid and turbidite beds. Whilst the grain size curves are largely distinctive for the different flow types (summarised in Fig. 15), SK2 although described as a hybrid bed has much the same character as a turbidite, albeit slightly enriched in coarser grains and with a more clay rich top (see Table 1).

167x167mm (300 x 300 DPI)

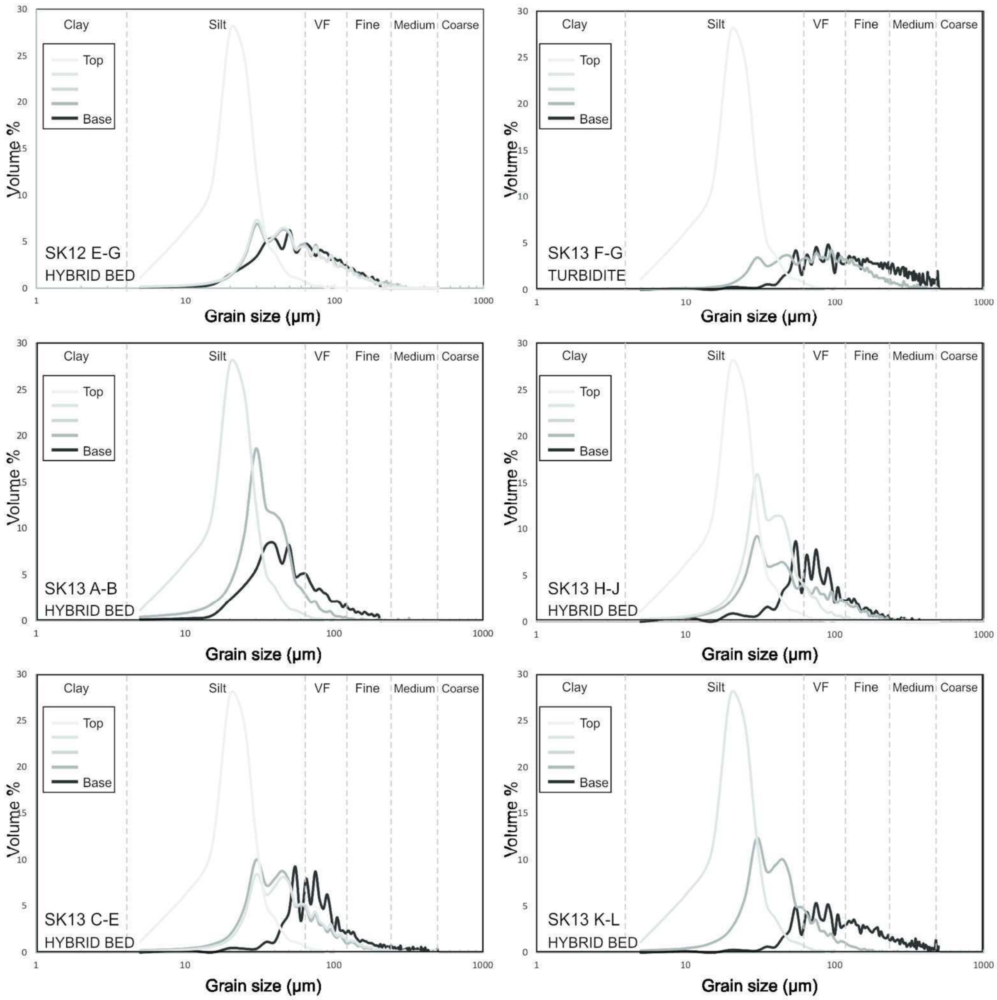

Figure 15. Representative grains-size distribution for deposits described as A) turbidites and B) hybrid beds. Turbidites are characterised by positively (fine) skewed lower bed divisions, and typically symmetrical upper divisions; in contrast, hybrid beds are characterised by negative (coarse) skewed lower divisions and symmetrical to coarse upper divisions.

167x167mm (300 x 300 DPI)

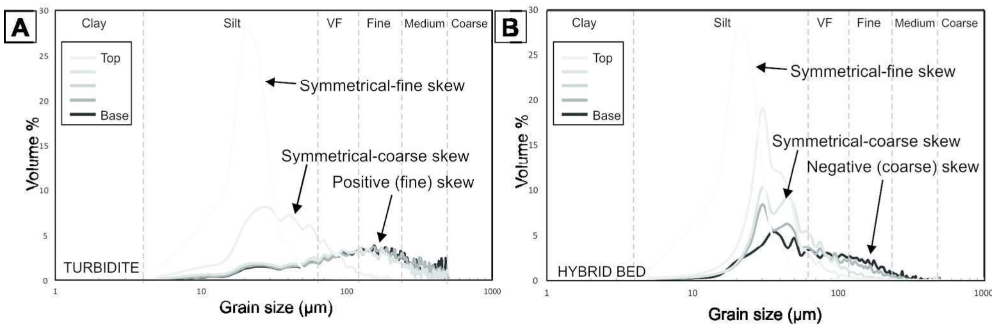

Figure 15. Representative grains size distributions for deposits described as A) turbidites and B) hybrid beds. Turbidites are characterized by positively (fine) skewed lower bed divisions, and typically symmetrical upper divisions; in contrast, hybrid beds are characterized by negative (coarse) skewed lower divisions and symmetrical to coarse upper divisions.

171x56mm (300 x 300 DPI)

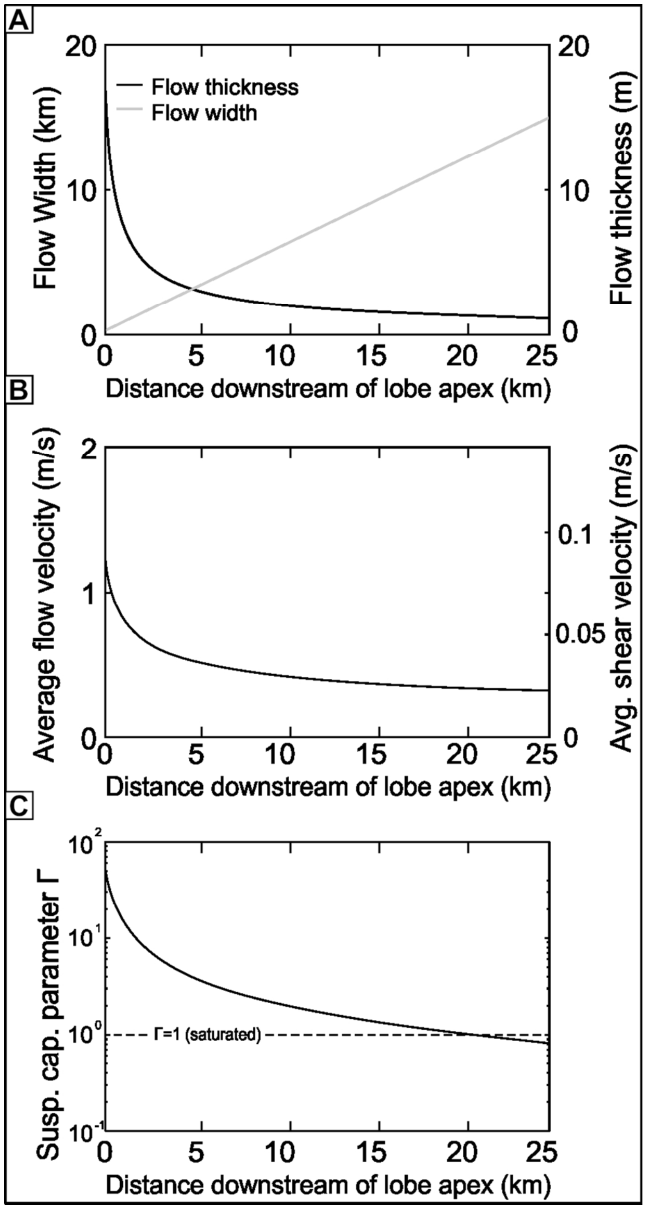

Figure 16. Flow parameters along lobe length for a scenario where channel width is 250 m; channel depth and initial flow thickness are 13 m and 17 m respectively; flow concentration is 5%; slope is 1.5*10-3; lobe width is 15 km; lobe length is 25km. (A) Flow width increases linearly over the lobe length from the channel width at the lobe apex to the full lobe width. Flow thickness decreases rapidly proximally, and more slowly distally. (B) Average velocity (left y-axis) and bed-shear velocity (right y-axis). Plots overlap because the drag coefficient has been used to normalise the right y-axis according to Eq. (4). (C) Suspension capacity parameter Γ is much larger than 1 at the lobe apex, indicating undersaturated near-bed conditions, reaches the threshold value of Γ =1 21 km downstream of the lobe apex, and Γ <1, leading to turbulence suppression, downstream of 21 km.

80x150mm (300 x 300 DPI)

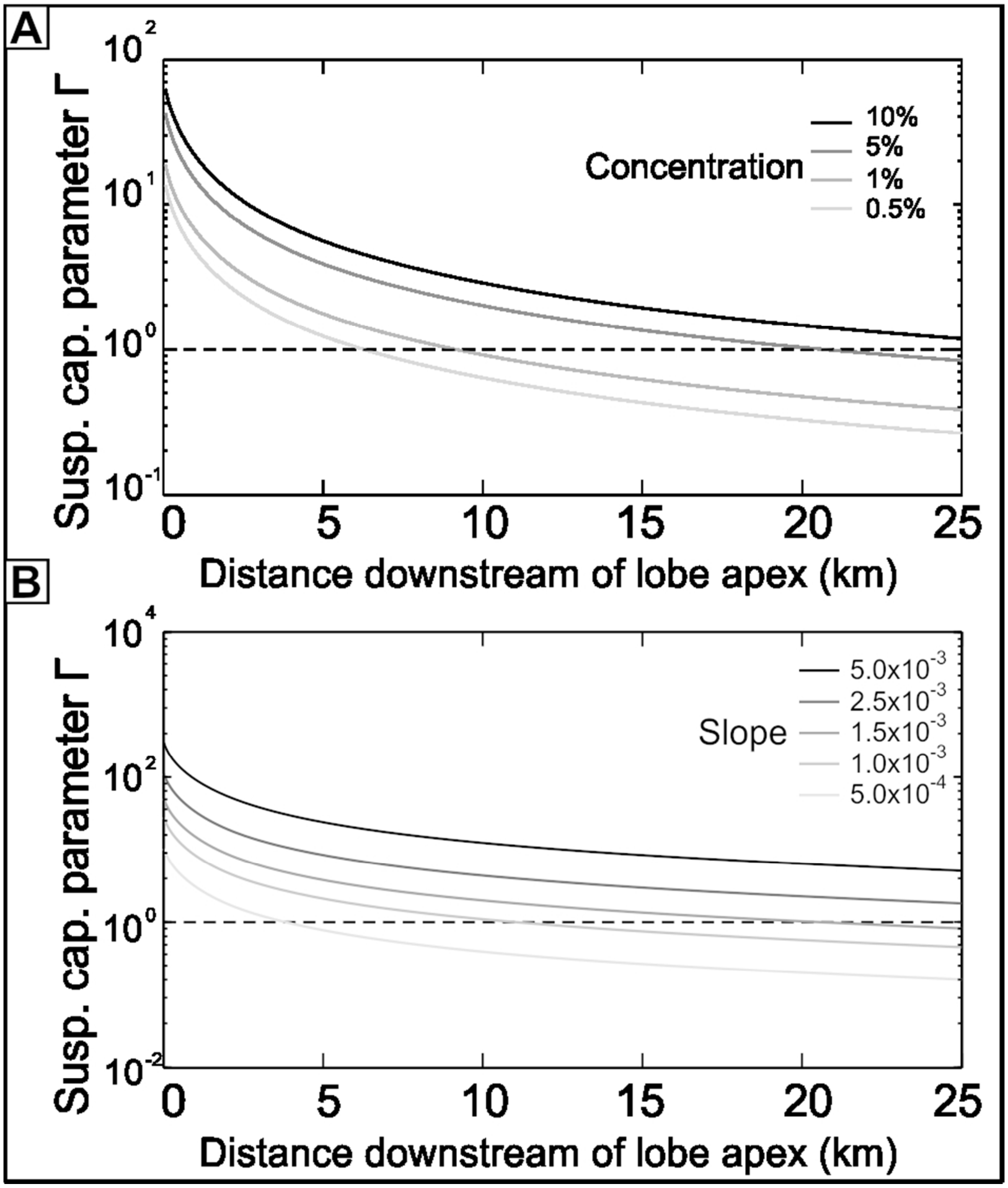

Figure 17. The sensitivity of the downstream evolution of Γ to different estimations for inlet concentration and slope. (A) Sediment concentrations of 10%, 5%, 1%, and 0.5%; for a given slope, the distance to flow transformation increases with increasing sediment concentration. (B) Slope gradients of 5.0*10-3, 2.5*10-3, 1.5*10-3, 1*10-3, and 5.0*10-4; for a given concentration, the distance to flow transformation increases with increasing slope.

80x94mm (300 x 300 DPI)

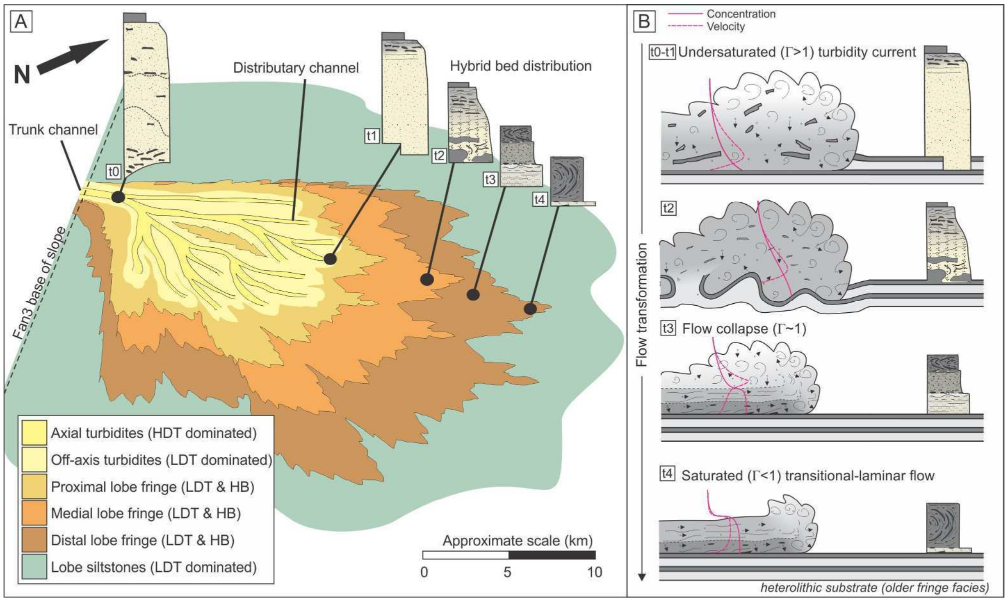

Figure 18. A) Schematic perspective/plan view of Fans 3. The distribution of hybrid beds is illustrated with schematic logs (see 'B'), but note that the fan fringe is not limited to hybrid beds, low-density turbidites are also common. At t0, in the trunk channels, flows are undersaturated with respect to the flow suspension capacity ($\Gamma > 1$) and strongly erosional; high density turbidites are amalgamated and can be mudstone-clast rich. B) Summary diagram of flow evolution and deposit type for flows in the fringe area which start out, at t1, fully turbulent and well mixed and undersaturated ($\Gamma > 1$), capable of eroding and entraining substrate. As flows decelerate from the channel-lobe transition (t2), shear stress exerted on the bed decreases, leaving substrate interaction preserved and resultant deposits clast and mud rich. Further deceleration and enrichment in cohesive and fine grained material (t3) results in the concentration profile becoming increasingly stratified and, when flows drop below the critical value of $\Gamma=1$ they are oversaturated and suspension capacity is lost. A dense lower layer forms, which continues to move downstream owing to its high water content (due to clays and very fine silts), grains are supported by yield strength but coarser grains settle resulting in a relatively well sorted sand fraction within a mud-rich matrix. Overlying layers are muddier and less well sorted. The formation of this high concentration lower boundary layer flow inhibits the transmission of turbulent kinetic energy into the upper part of the flow and turbulence is rapidly dissipated (t4).

223x132mm (300 x 300 DPI)

	Id	SK2A	SK2B	SK2C	SK2D	SK3A	SK3B	SK3C	SK3D	SK3E	SK3F	SK4A	SK4B	SK4C	SK4D	SK4E	SK4F	SK4G	SK4H	SK4I
	Bed Type	HB-base	HB	HB	HB-top	TURB-base	TURB	TURB-top	AMAL-base	AMAL	AMAL-top	HB-base	HB	HB	HB-top	HB-base	HB	HB	HB	HB-top
Mineral Mass (%)	Quartz	46.25	44.95	41.84	31.86	46.07	47.38	38.78	44.48	42.99	42.77	38.08	32.08	37.00	30.67	41.96	34.79	37.51	36.27	30.18
	Plagioclase	34.87	35.53	33.42	28.82	35.49	35.47	33.12	33.32	34.80	34.74	32.73	28.36	31.88	24.83	32.38	28.37	30.81	29.93	25.15
	K-Feldspar	2.00	1.89	1.97	2.01	1.91	1.81	1.80	2.05	1.72	2.16	2.40	2.11	2.54	1.30	2.37	1.80	1.80	1.94	1.34
	Muscovite	1.01	0.96	0.98	1.82	0.90	1.00	1.45	1.02	1.03	1.02	1.35	1.87	1.35	1.73	1.18	1.52	1.52	1.58	1.63
	Illite	9.02	9.78	12.81	22.28	8.67	8.30	15.31	9.42	8.83	9.84	15.79	25.69	17.36	32.89	12.93	24.55	18.24	19.52	31.98
	Chlorite	3.78	3.25	5.15	8.03	3.71	3.41	6.05	6.68	6.26	4.46	5.31	5.21	5.92	4.40	4.74	4.64	5.94	6.44	5.22
	Other clays	0.81	1.34	1.27	1.84	1.11	0.81	1.40	1.10	0.87	0.76	2.07	1.69	1.58	1.50	1.86	1.75	1.61	1.73	1.99
	Calcite	0.11	0.10	0.29	0.13	0.00	0.00	0.00	0.00	1.76	2.38	0.00	0.00	0.00	0.00	0.00	0.00	0.00	0.00	0.02
	Rutile	0.99	0.88	0.95	1.71	0.82	0.75	0.91	0.76	0.76	0.82	0.98	1.51	0.96	1.06	0.92	1.17	1.15	1.20	0.88
	Apatite	0.39	0.33	0.37	0.58	0.44	0.42	0.51	0.40	0.35	0.33	0.45	0.55	0.47	0.67	0.46	0.53	0.55	0.55	0.62
	Zircon	0.05	0.02	0.02	0.02	0.06	0.04	0.03	0.07	0.07	0.02	0.02	0.03	0.02	0.02	0.03	0.02	0.02	0.03	0.01
	Others	0.01	0.04	0.02	0.02	0.27	0.03	0.03	0.02	0.02	0.01	0.02	0.02	0.04	0.05	0.06	0.02	0.01	0.01	0.02
	Unclassified	0.71	0.94	0.90	0.89	0.57	0.56	0.63	0.68	0.54	0.67	0.81	0.89	0.88	0.90	1.12	0.84	0.83	0.80	0.96
Mineral Volume (%)	Quartz	46.71	45.42	42.35	32.56	46.56	47.79	39.33	44.93	43.42	43.21	38.66	32.78	37.56	31.39	42.52	35.48	38.14	36.92	30.87
	Plagioclase	35.28	35.97	33.90	29.51	35.93	35.84	33.65	33.72	35.21	35.16	33.30	29.03	32.42	25.46	32.88	28.99	31.39	30.53	25.77
	K-Feldspar	2.07	1.96	2.04	2.11	1.98	1.88	1.87	2.12	1.79	2.24	2.50	2.21	2.64	1.36	2.46	1.89	1.87	2.02	1.41
	Muscovite	0.95	0.90	0.92	1.73	0.84	0.94	1.37	0.96	0.97	0.96	1.28	1.77	1.28	1.64	1.11	1.44	1.44	1.49	1.55
	Illite	8.70	9.43	12.38	21.73	8.36	7.99	14.82	9.08	8.51	9.49	15.30	25.06	16.83	32.14	12.51	23.90	17.70	18.97	31.22
	Chlorite	3.78	3.25	5.17	8.12	3.71	3.41	6.07	6.68	6.26	4.46	5.34	5.28	5.95	4.46	4.76	4.69	5.99	6.49	5.29
	Other clays	0.73	1.18	1.13	1.64	0.98	0.73	1.24	0.97	0.77	0.67	1.82	1.53	1.41	1.38	1.65	1.58	1.43	1.54	1.82
	Calcite	0.11	0.10	0.28	0.13	0.00	0.00	0.00	0.00	1.72	2.33	0.00	0.00	0.00	0.00	0.00	0.00	0.00	0.00	0.02
	Rutile	0.62	0.55	0.59	1.08	0.51	0.47	0.57	0.47	0.47	0.51	0.62	0.95	0.60	0.67	0.58	0.73	0.72	0.76	0.56
	Apatite	0.32	0.27	0.31	0.48	0.37	0.35	0.42	0.34	0.29	0.27	0.37	0.46	0.40	0.56	0.38	0.44	0.46	0.46	0.52
	Zircon	0.03	0.01	0.01	0.01	0.03	0.03	0.02	0.04	0.04	0.01	0.01	0.01	0.01	0.01	0.02	0.01	0.01	0.02	0.01
	Others	0.01	0.03	0.02	0.02	0.16	0.02	0.02	0.02	0.02	0.01	0.01	0.02	0.03	0.04	0.04	0.01	0.01	0.01	0.02
	Unclassified	0.70	0.93	0.89	0.88	0.56	0.55	0.62	0.67	0.53	0.66	0.80	0.88	0.87	0.89	1.10	0.83	0.82	0.79	0.95

	Id	SK12A	SK12B	SK12C	SK12D	SK12E	SK12F	SK12G	SK13A	SK13B	SK13C	SK13D	SK13E	SK13F	SK13G	SK13H	SK13I	SK13J	SK13K	SK13L	SK14
	Bed Type	HB-base	HB	HB	HB-top	HB-base	HB	HB-top	HB-base	HB-top	HB-base	HB	HB-top	TURB-base	TURB-top	HB-base	HB	HB-top	HB-base	HB-top	AMAL-mid
Mineral Mass (%)	Quartz	38.62	35.88	36.12	35.27	41.46	36.61	35.96	43.35	34.39	44.40	34.73	36.94	48.16	38.40	31.53	30.94	29.82	45.21	30.74	42.94
	Plagioclase	28.71	27.28	29.11	26.11	32.18	30.57	29.40	29.25	24.56	31.18	27.06	29.12	33.65	32.52	26.27	26.87	27.02	34.36	28.18	35.90
	K-Feldspar	2.53	2.43	1.96	1.75	1.97	2.01	2.00	1.85	1.58	2.08	1.87	1.87	1.79	2.00	2.21	2.14	1.74	2.00	1.60	1.51
	Muscovite	1.50	1.92	2.40	1.78	1.34	1.68	2.00	1.26	1.65	1.12	1.94	1.86	1.17	2.16	1.78	2.10	2.22	1.36	2.25	1.15
	Illite	19.61	22.43	20.07	24.58	14.04	19.25	19.98	15.00	28.62	12.45	22.94	20.11	6.90	13.25	28.59	28.08	26.70	8.11	25.08	10.70
	Chlorite	5.13	5.09	5.93	6.23	5.39	5.37	5.23	5.63	5.35	5.21	5.67	5.66	4.36	7.22	4.77	5.65	7.40	4.93	7.32	5.26
	Other clays	1.80	2.09	1.91	2.06	1.39	2.02	2.38	1.57	1.84	1.84	2.43	2.19	1.26	1.92	1.73	1.97	2.46	1.44	2.09	1.02
	Calcite	0.00	0.46	0.23	0.00	0.00	0.00	0.00	0.00	0.00	0.00	0.00	0.00	0.00	0.00	0.00	0.00	0.01	0.38	0.01	0.01
	Rutile	0.80	0.85	0.86	0.95	0.88	0.82	0.81	0.75	0.97	0.66	0.87	0.80	0.63	0.68	0.86	0.92	0.97	0.59	1.00	0.64
	Apatite	0.47	0.45	0.51	0.55	0.50	0.45	0.45	0.50	0.54	0.47	0.47	0.47	0.34	0.41	0.50	0.50	0.55	0.38	0.56	0.39
	Zircon	0.02	0.02	0.02	0.02	0.03	0.02	0.02	0.02	0.02	0.02	0.02	0.02	0.02	0.02	0.02	0.02	0.02	0.03	0.03	0.03
	Others	0.14	0.22	0.07	0.14	0.05	0.39	0.46	0.08	0.06	0.08	0.73	0.05	0.27	0.17	0.05	0.16	0.30	0.05	0.33	0.02
	Unclassified	0.67	0.89	0.81	0.56	0.76	0.81	1.29	0.73	0.42	0.50	1.27	0.90	1.45	1.25	1.70	0.65	0.80	1.16	0.79	0.44
Mineral Volume (%)	Quartz	39.24	36.53	36.74	35.97	42.00	37.23	36.61	43.92	35.12	44.93	35.45	37.56	48.58	38.92	32.19	31.60	30.49	45.62	31.41	43.36
	Plagioclase	29.23	27.83	29.66	26.68	32.67	31.15	29.99	29.70	25.13	31.61	27.67	29.67	34.00	33.02	26.86	27.49	27.67	34.73	28.85	36.32
	K-Feldspar	2.63	2.53	2.05	1.83	2.04	2.09	2.09	1.93	1.66	2.16	1.96	1.95	1.86	2.08	2.31	2.24	1.83	2.07	1.68	1.56
	Muscovite	1.42	1.81	2.27	1.68	1.26	1.59	1.89	1.18	1.57	1.05	1.84	1.76	1.09	2.03	1.69	1.99	2.11	1.27	2.14	1.08
	Illite	19.02	21.80	19.49	23.93	13.58	18.69	19.41	14.51	27.90	12.02	22.35	19.52	6.64	12.82	27.85	27.37	26.05	7.81	24.46	10.32
	Chlorite	5.16	5.13	5.98	6.29	5.41	5.41	5.27	5.66	5.41	5.22	5.73	5.70	4.36	7.25	4.82	5.72	7.49	4.92	7.41	5.26
	Other clays	1.63	1.96	1.77	1.89	1.26	1.88	2.26	1.43	1.68	1.65	2.31	2.01	1.19	1.75	1.58	1.82	2.27	1.32	1.91	0.91
	Calcite	0.00	0.45	0.22	0.00	0.00	0.00	0.00	0.00	0.00	0.00	0.00	0.00	0.00	0.00	0.00	0.00	0.01	0.38	0.01	0.01
	Rutile	0.50	0.54	0.54	0.60	0.55	0.52	0.51	0.47	0.61	0.41	0.55	0.50	0.39	0.42	0.54	0.58	0.61	0.37	0.63	0.40
	Apatite	0.39	0.37	0.43	0.46	0.42	0.38	0.38	0.42	0.45	0.39	0.39	0.39	0.28	0.34	0.42	0.42	0.46	0.32	0.47	0.32
	Zircon	0.01	0.01	0.01	0.01	0.02	0.01	0.01	0.01	0.01	0.01	0.01	0.01	0.01	0.01	0.01	0.01	0.01	0.02	0.01	0.01
	Others	0.09	0.15	0.05	0.09	0.03	0.25	0.30	0.06	0.04	0.05	0.48	0.04	0.17	0.11	0.03	0.11	0.20	0.03	0.22	0.02
	Unclassified	0.66	0.88	0.80	0.55	0.75	0.80	1.28	0.72	0.42	0.49	1.26	0.89	1.42	1.23	1.69	0.64	0.80	1.13	0.78	0.44

Table 1. Mineralogical composition of samples analysed using QEMSCAN. Heavy outlines mark individual beds, which are classified here as hybrid beds (HB), turbidites (TURB) and thick amalgamated sandstone – see text (AMAL), the lowermost and uppermost samples for each bed are marked (-base and -top respectively).

381x259mm (300 x 300 DPI)

Sample name	Bed Type	Grain count	Vectorial mean (M)	Mean vector magnitude (R)	Vectorial concentration (K)	Distribution type (0.05)
2A	TFD	55243	27.10	0.11	0.23	Von Mises
2B	TFD	59868	19.71	0.18	0.36	Von Mises
2C	TFD	59245	1.32	0.09	0.17	Von Mises
2D	TFD	101249	14.04	0.25	0.52	Von Mises
3A	Turbidite	73993	159.35	0.10	0.21	Von Mises
3B	Turbidite	61991	136.56	0.02	0.04	Uniform
3C	Turbidite	146406	9.15	0.29	0.60	Von Mises
3D	Amal. Turbidite	48116	5.69	0.12	0.24	Von Mises
3E	Amal. Turbidite	44879	20.18	0.17	0.34	Von Mises
3F	Amal. Turbidite	56065	26.47	0.07	0.13	Uniform
4A	TFD	33527	22.88	0.16	0.32	Von Mises
4B	TFD	88577	176.47	0.19	0.39	Von Mises
4C	TFD	80043	1.78	0.19	0.39	Von Mises
4D	TFD	35400	8.86	0.34	0.72	Von Mises
4E	TFD	67770	161.69	0.17	0.34	Von Mises
4F	TFD	71208	10.71	0.22	0.45	Von Mises
4G	TFD	113744	175.94	0.22	0.46	Von Mises
4H	TFD	98892	9.45	0.28	0.57	Von Mises
4I	TFD	37427	178.45	0.33	0.69	Von Mises
12A	TFD	43312	1.19	0.25	0.51	Von Mises
12B	TFD	46508	13.38	0.31	0.65	Von Mises
12C	TFD	40441	167.34	0.17	0.35	Von Mises
12D	TFD	8246	7.18	0.35	0.75	Von Mises
12E	TFD	74736	21.73	0.28	0.59	Von Mises
12F	TFD	38182	6.53	0.22	0.45	Von Mises
12G	TFD	56020	176.10	0.12	0.25	Von Mises
13A	TFD	53342	2.39	0.26	0.53	Von Mises
13B	TFD	5934	8.84	0.32	0.68	Von Mises
13C	TFD	32897	10.16	0.23	0.48	Von Mises
13D	TFD	27875	158.87	0.24	0.50	Von Mises
13E	TFD	45056	176.67	0.24	0.48	Von Mises
13F	Turbidite	32994	162.82	0.14	0.27	Von Mises
13G	Turbidite	70501	151.62	0.05	0.10	Uniform
13H	TFD	9710	12.33	0.22	0.45	Von Mises
13I	TFD	28323	176.61	0.27	0.56	Von Mises
13J	TFD	6768	5.96	0.33	0.71	Von Mises
13K	TFD	13707	2.09	0.13	0.27	Uniform
13L	TFD	22479	5.79	0.25	0.53	Von Mises
14A	Amal .Turbidite	59829	175.50	0.19	0.38	Von Mises

Table 2. Grain fabric data. Heavy outlines mark individual beds, which are classified here as HB (hybrid bed), TURB (turbidite) and AMAL (thick amalgamated sandstone – see text).

265x182mm (300 x 300 DPI)